

## TOPICAL REVIEW

# Strong correlations in a nutshell

Michel Ferrero<sup>1</sup>, Lorenzo De Leo<sup>1,2</sup>, Philippe Lecheminant<sup>3</sup> and Michele Fabrizio<sup>4,5</sup>

<sup>1</sup> Center de Physique Théorique, Ecole Polytechnique, 91128 Palaiseau Cedex, France

<sup>2</sup> Center for Material Theory, Serin Physics Laboratory, Rutgers University, 136 Frelinghuysen Road, Piscataway, NJ 08854-8019, USA

<sup>3</sup> Laboratoire de Physique Théorique et Modélisation, Université de Cergy-Pontoise, CNRS UMR 8089, 2 Avenue Adolphe Chauvin, 95302, Cergy-Pontoise, France

<sup>4</sup> International School for Advanced Studies (SISSA), and INFN-Democritos, National Simulation Center, I-34014 Trieste, Italy

<sup>5</sup> The Abdus Salam International Center for Theoretical Physics (ICTP), PO Box 586, I-34014 Trieste, Italy

Received 26 June 2007, in final form 9 August 2007

Published 8 October 2007

Online at [stacks.iop.org/JPhysCM/19/433201](http://stacks.iop.org/JPhysCM/19/433201)

## Abstract

We present the phase diagram of clusters made of two, three and four coupled Anderson impurities. All three clusters share qualitatively similar phase diagrams that include Kondo screened and unscreened regimes separated by almost critical crossover regions reflecting the proximity to barely avoided critical points. This suggests the emergence of universal paradigms that apply to clusters of arbitrary size. We discuss how these crossover regions of the impurity models might affect the approach to the Mott transition within a cluster extension of dynamical mean field theory.

(Some figures in this article are in colour only in the electronic version)

## Contents

1. Introduction	2
1.1. Competing screening mechanisms in Anderson impurity models	4
1.2. Impurity models and dynamical mean field theory	5
2. The impurity dimer	7
2.1. Dynamical behavior of the impurity dimer	10
3. The impurity trimer	15
3.1. CFT preliminaries for the trimer	16
3.2. Fixed points in the trimer phase diagram	17
3.3. Dynamical properties of the trimer	20
4. The impurity tetramer	21
4.1. CFT preliminaries for the tetramer	21
4.2. Fixed points in the tetramer phase diagram	23
5. Discussion and conclusions	27

<a href="#">Acknowledgments</a>	28
<a href="#">Appendix. CFT at work</a>	28
<a href="#">References</a>	34

### Acronyms and main notation

$W$	Non-interacting electron bandwidth
$U$	Hubbard on-site repulsion
$T_F^*$	Quasi-particle effective Fermi temperature
$\Gamma$	Impurity hybridization width
$T_K$	Kondo temperature
$\rho(\epsilon)$	Impurity density of states
$\Sigma(i\omega)$	Impurity self-energy in Matsubara frequencies
MIT	Mott metal-to-insulator transition
DMFT	Dynamical mean field theory
NRG	Wilson's numerical renormalization group
CFT	Conformal field theory
DOS	Single-particle density of states

## 1. Introduction

The Mott metal-to-insulator transition [1, 2] emerges out of the competition between the opposite tendencies of the electrons to delocalize throughout the lattice in order to maximize the band energy gain and their mutual Coulomb repulsion which, on the contrary, tends to suppress valence fluctuations by localizing the carriers. If the band energy gain, which can be identified with the ‘bare’ bandwidth  $W$ , is small enough with respect to the short range Coulomb repulsion, commonly parametrized by an on-site Hubbard  $U$ , and the average electron density per site is integer, charge gets localized and the system is a Mott insulator; otherwise it remains metallic.

Despite its intuitive nature, the Mott phenomenon is extremely difficult to study because it is inherently non-perturbative and because it escapes any simple single-particle description. Those can only deal with band insulators, characterized by an energy gap separating totally filled from unfilled bands. The simplest example of a Mott insulator is provided by the single-band Hubbard model at half-filling, which always has an insulating phase at sufficiently large repulsion. Yet, in order to make this phase appear for instance in Hartree–Fock theory, one is obliged to assume an antiferromagnetic order parameter that doubles the unit cell so as to fulfill the necessary requirement for a band insulator—an even number of electrons per unit cell. With this trick, the Mott transition is effectively turned into a metal to band insulator transition driven by magnetism. In reality, local moments form and eventually order as a consequence of charge localization by the Mott phenomenon. This distinction might look pedantic since the ground state is anyway both insulating and magnetic, but in fact it is not, as we are going to argue by the qualitative behavior of the entropy in the Mott insulator and in the contiguous metal.

In figure 1, we sketch the typical temperature dependence of the entropy deep inside a Mott insulating phase,  $U \gg W$ . At high temperature,  $T \lesssim U$ , valence fluctuations are suppressed and the local charge gets locked to some fixed value  $n_0$ . Yet, all local electronic configurations with  $n_0$  electrons are thermally occupied with equal probability, leading to a constant entropy regime that could be identified as the ideal Mott insulator, where charge degrees of freedom are frozen while all other degrees of freedom, in particular spin, are

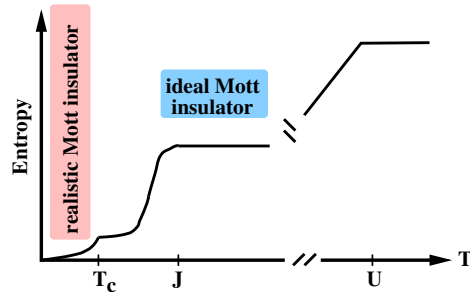


Figure 1. Qualitative behavior of the entropy in a Mott insulator.

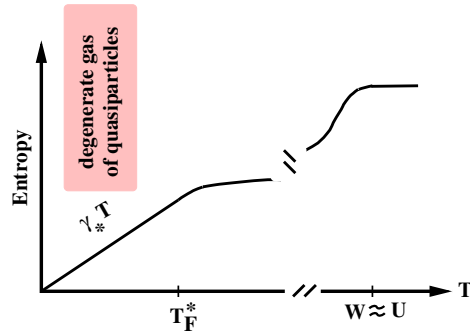


Figure 2. Qualitative behavior of the entropy of a strongly correlated metal.

completely free. However, at some lower temperature, other energy scales come into play whose role is to lock these additional degrees of freedom, namely to favor one or several among all the local electronic configurations with  $n_0$  electrons. These energy scales may include for instance the on-site Coulomb exchange, responsible for the Hund’s rules, the inter-site direct exchange or superexchange, the crystal field, the coupling to the lattice, etc. We will collectively denote these energy scales by  $J$ , which may be identified as the temperature below which the entropy of the residual degrees of freedom of the ideal Mott insulator starts to be suppressed. Consequently, at low temperature, a realistic insulating phase is established, which is commonly accompanied by a symmetry breaking phase transition at  $T = T_c \leq J$ , for instance a magnetic ordering, a collective Jahn–Teller distortion, etc. Below  $T_c$ , the entropy decreases to zero as  $T \rightarrow 0$ , generically faster than linearly. For instance, in the half-filled single-band Hubbard model, the ideal Mott insulator corresponds to a regime in which each site is singly occupied but its spin can be with equal probability either up or down, leading to an entropy  $\ln 2$  per site. However, below a temperature of the order of the inter-site spin exchange, the  $\ln 2$  entropy decreases until the system crosses a magnetic phase transition, below which its entropy vanishes according to the dimensionality of the system and to the dispersion relation of the spin waves.

Recently, an amount of research activity has focused on the possibility that different symmetry broken phases may compete in the insulator, leading to exotic low temperature phenomena [3]. Here, we will completely discard this event and concentrate on a different competition which emerges in the metallic phase adjacent the Mott insulator.

In figure 2, we draw how the entropy versus temperature might look like for a strongly correlated Fermi liquid-like metal, assuming that no symmetry breaking intervenes down to

zero temperature. As before, we expect that the charge entropy is, this time only partially, reduced at some high temperature of order  $U \simeq W$ . The rest of it, as well as the entropy of the other degrees of freedom, are instead suppressed by the formation of the degenerate quasi-particle gas. This occurs below a temperature  $T_F^*$ , that can be identified as the effective quasi-particle Fermi temperature. Since quasi-particles carry the same quantum numbers as the electrons, the entropy quenching involves all degrees of freedom at once, including the charge. Below  $T_F^*$  the entropy vanishes linearly,  $S(T) \simeq \gamma_* T$ , with a specific heat coefficient  $\gamma_*$  usually larger than its non-interacting value  $\gamma \sim 1/W$ .

Let us suppose that the Mott transition (MIT) were continuous and try to guess how that might happen from the point of view of the entropy. Obviously, since quasi-particles disappear in the Mott insulator,  $T_F^*$  has to vanish at the MIT. Therefore, sufficiently close to the MIT, the quasi-particle Fermi temperature  $T_F^*$  must become smaller than  $J$ . When this happens we should expect, by continuity with the insulating side, that part of the spin entropy gets suppressed already at temperatures of order  $J$ , above the onset of Fermi degeneracy. This amounts to some kind of pseudo-gap opening above  $T_F^*$ , which is at odds with the conventional Landau–Fermi liquid theory. One way out, apart from a first-order MIT, is that something new occurs when  $T_F^* \simeq J$ . Indeed, the presence of  $J$  provides the metallic phase with an alternative mechanism to freeze spin degrees of freedom independently of the charge ones, a mechanism that becomes competitive with the onset of a degenerate quasi-particle gas when  $T_F^* \simeq J$ . This competition is likely to lead to an instability of the Landau–Fermi liquid towards a low temperature symmetry broken phase (this happens in the insulating side), but may also signal a real breakdown of Fermi liquid theory.

Notice that, unlike the competition between different symmetry broken Mott insulating phases, which requires a fine tuning of the Hamiltonian parameters that may only accidentally occur in real materials, this other type of competition—whose effects have not been discussed in the literature before to the extent we believe they deserve—should be encountered whenever it is possible to move gradually from a Mott insulator into a metallic phase, for instance by doping or by pressure. We also know several examples where this competition is argued to be at the origin of interesting phenomena. For instance, in heavy fermion materials the Kondo effect, favoring the formation of a coherent band of heavy quasi-particles, competes with the RKKY (Ruderman–Kittel–Kasuya–Yosida) interaction (for a comprehensive review see e.g. [4]). Here this competition is supposedly the key to understand the anomalies which appear at the transition between the heavy fermion paramagnet and the magnetically ordered phase [5–7].

### *1.1. Competing screening mechanisms in Anderson impurity models*

The heavy fermion example is a particularly pertinent one to introduce the subject of this review. Indeed, the competition between Kondo effect and RKKY coupling has interesting consequences not only in the periodic Anderson model but already at the level of Anderson impurity models.

For instance, the phase diagram of two spin-1/2 impurities coupled to a conduction bath and mutually by a direct antiferromagnetic exchange has two limiting regimes: one where each impurity is independently Kondo screened by the conduction electrons; and another where the exchange locks the impurity spins into a singlet state, now transparent to the conduction electrons. Under particular circumstances—the two involved scattering channels must be independently coupled each to one impurity—these two regimes are separated by a quantum critical point, at which non-Fermi liquid behavior emerges [8–12].

The phase diagram grows richer when one consider three antiferromagnetically coupled spin-1/2 impurities [13, 14]. Here, besides a Kondo screened regime, there are other phases

where the direct exchange prevails, but is unable to fully quench all impurity degrees of freedom. This leads to stable non-Fermi liquid phases analogous to overscreened multi-channel Kondo models [15, 16]. These impurity cluster models are interesting not only as simple attempts towards an understanding of the fully periodic Anderson model, but also because compact cluster of impurities are achievable experimentally by adsorbing atoms on metallic surfaces. Trimers of Cr atoms have already been realized on gold surfaces [17], which has actually motivated the most recent theoretical activity on impurity trimers [18–20, 14]. In this context, the major task is to identify those phases which are stable towards perturbations generically present on metallic surfaces. Therefore the quantum critical points that separate stable phases are of minor interest from an experimental point of view, as they require such a fine tuning that is extremely unlikely to occur in physical systems.

### 1.2. Impurity models and dynamical mean field theory

Unstable critical points arise when the competition between Kondo screening and RKKY coupling is maximum. This is nothing but the impurity counterpart of the situation in which  $T_F^* \simeq J$  we previously met in connection with the Mott transition. This weak analogy turns into an actual equivalence within the so-called dynamical mean field theory (DMFT) [21], the quantum analogue of classical mean field theory which, like the latter, is exact for infinite coordination lattices. In this limit, the single-particle self-energy becomes fully local but maintains a non-trivial time dependence, obtained within DMFT by solving an auxiliary single-impurity Anderson model that is designed so as to have an impurity self-energy that coincides with the local self-energy of the lattice model. This requirement translates into an impurity model identified by the same local interaction as the lattice model and by a coupling to a conduction bath that must be self-consistently determined. The single-site formulation of DMFT has provided a lot of useful information about the Mott transition *per se*, disentangled from magnetism or whatever symmetry breaking occurs in the insulating state. However, even though single-site DMFT can account in a Hartree–Fock manner for simple magnetic phases on bipartite lattice, it is inadequate to study our anticipated competition. For instance, it misses precursor effects in the paramagnetic phase close to the magnetic phase transition, caused by inter-site processes which disappear in infinite coordination lattices. For this reason, several extensions of DMFT have been recently proposed to include short range spatial correlations [22–26]. In these novel versions, the lattice model is mapped onto a cluster of Anderson impurities, subject to self-consistency conditions.

The physics of the Anderson impurity model turned out to be a precious guideline to interpret single-site DMFT results [21]. Similarly, we expect that the preliminary knowledge of the general properties of impurity clusters is useful, perhaps even necessary, in connection with any cluster extension of DMFT. However, apart from few exceptions [8, 13], little is known about impurity clusters. In addition, since models of impurity clusters involve many intra-impurity and inter-impurity energy scales, it is not *a priori* evident that there should be a common interpreting framework like the Kondo physics in the single-impurity case.

This is actually the purpose of this review. Specifically, we are going to present the phase diagram of the simplest among impurity clusters, namely dimers, trimers and tetramers, that could be used to implement a cluster DMFT calculation on strongly correlated models. Besides our main objective to identify the common features among different clusters, which should presumably play the most significant role in a DMFT approach, we will also try to argue how much of the impurity cluster physics might survive the DMFT self-consistency, hence the possible consequences on the phase diagram of the lattice models. Needless to say, the interest in impurity clusters goes beyond its possible relevance to strongly correlated models

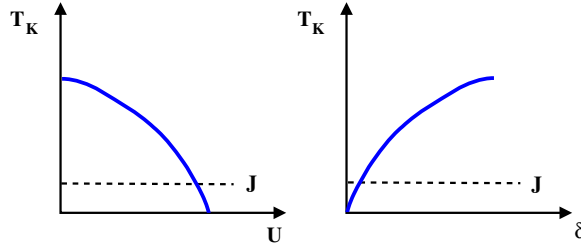


**Figure 3.** Behavior versus  $U$  and doping  $\delta$  of the quasiparticle Fermi temperature,  $T_F^*$ , which translates within DMFT into the Kondo temperature  $T_K$  of the effective impurity model.  $J$  is an effective intra-cluster energy scale.

near a Mott transition. As we previously mentioned, these clusters may be experimentally realized on metallic surfaces or, eventually, by arranging quantum dots in proper geometries. Moreover, these models represent a theoretical challenge by themselves, which requires the full machinery of Wilson's numerical renormalization group (NRG) [27–29] and conformal field theory (CFT) [30] for a detailed comprehension.

Before entering into the details of our calculations, it is worth briefly presenting the physical idea that guided this work. First of all, let us recall some basic facts of the single-site DMFT mapping onto impurity models. Within this mapping, the quasi-particle effective Fermi temperature,  $T_F^*$ , translates into the Kondo temperature,  $T_K$ , of the impurity model. The self-consistency condition causes  $T_K$  to vanish at a finite value of  $U$ , which signals, in the lattice counterpart, the onset of the Mott transition. This also implies that the metallic phase just prior to the Mott transition translates into an Anderson impurity model deep inside the Kondo regime, with a very narrow Kondo resonance and pre-formed Hubbard side-bands [21]. The same behavior should occur even when dealing with a cluster of impurities, which should therefore translate into a cluster of Kondo impurities. The novelty stems from the other energy scales which we collectively denoted as  $J$ , and that take care of quenching in the Mott insulator the degrees of freedom other than the charge. Indeed, near the Mott transition,  $J$  translates into additional processes, like for instance a direct exchange between the impurity spins, which tend to remove, completely or partially, the degeneracy of the cluster. Consequently,  $J$  competes with the Kondo effect, an agent that takes more advantage the more degenerate the impurity cluster ground state.

We notice that this competition is always active in impurity clusters, while it is commonly absent in single-impurity models except in multi-orbital cases [31, 32] whose physics is in fact close to clusters. We believe that this additional ingredient is precisely the common denominator of all impurity cluster models, which endows them with the capability of providing a more faithful description of a realistic Mott transition within DMFT.

Indeed, in the presence of the intra-cluster coupling  $J$ , the approach to the Mott transition changes as qualitatively shown in figure 3, with a Kondo temperature smoothly decreasing from its initial value  $W$  as  $U/W$  increases and becoming of order  $J$  just before the transition. Analogously, see also figure 3, starting from the Mott insulator and doping it,  $T_K$  will smoothly increase from its value  $T_K = 0$  at zero doping, until it will again cross a value of order  $J$ . In other words, any impurity cluster should experience, within DMFT, two different regimes. The first, when  $T_K \gg J$ , in which full Kondo screening takes place and the impurity density of states displays the usual Kondo resonance. In the lattice model, this regime translates into a conventional correlated metal. The second, when  $T_K \ll J$ , particularly close to the Mott transition, in which no or only partial Kondo screening occurs. Here the impurity density

of states is pseudo-gapped at the chemical potential. As we will show, these two regimes of the impurity cluster are generically separated by an almost critical crossover region that reflects the proximity to a true quantum critical point. How do the unscreened phase and the almost critical crossover region of the impurity cluster translate in the lattice model? The answer to this question would be simple if a true impurity critical point existed, as discussed in [33, 34]. Indeed, near a critical point, the impurity model displays strongly enhanced local susceptibilities, equivalently enhanced local irreducible four-leg vertices, in several instability channels. Within DMFT, the irreducible four-leg vertices, which enter the Bethe–Salpeter equations, coincide with the local ones [21]. Therefore, it is reasonable to argue that, after full DMFT self-consistency is carried out, these local instabilities may turn into symmetry breaking bulk instabilities that correspond to the same instability channels of the impurity critical point. However, establishing which one of these symmetry breakings really occurs requires full DMFT calculations, as it depends on other details, like for instance the nesting of the Fermi surface. These speculations have been tested with success by a DMFT analysis of a two-orbital Hubbard model [32]. Although these criticalities are, rigorously speaking, avoided in impurity cluster models pertinent to DMFT, still we believe that these models approach a critical point so closely that the physics does not change qualitatively.

In the following, we will describe in succession the case of dimer, trimer and tetramer clusters, and, in spite of their obvious differences, we will identify the universal aspects of the competition discussed above.

## 2. The impurity dimer

The simplest impurity cluster that is relevant to DMFT is a dimer described by the Hamiltonian

$$\begin{aligned} \mathcal{H} = & \sum_{a=1}^2 \sum_{\mathbf{k}\sigma} \epsilon_{\mathbf{k}} c_{a\mathbf{k}\sigma}^\dagger c_{a\mathbf{k}\sigma} + \sum_{\mathbf{k}\sigma} t_{\perp\mathbf{k}} \left( c_{1\mathbf{k}\sigma}^\dagger c_{2\mathbf{k}\sigma} + \text{H.c.} \right) - \sum_{a=1}^2 \sum_{\mathbf{k}\sigma} \left( V_{\mathbf{k}} c_{a\mathbf{k}\sigma}^\dagger d_{a\sigma} + \text{H.c.} \right) \\ & - t_{\perp} \sum_{\sigma} \left( d_{1\sigma}^\dagger d_{2\sigma} + \text{H.c.} \right) + \frac{U}{2} \sum_{a=1}^2 (n_a - 1)^2, \end{aligned} \quad (1)$$

where  $c_{a\mathbf{k}\sigma}^\dagger$  creates a conduction electron in channel  $a = 1, 2$  with momentum  $\mathbf{k}$ , energy  $\epsilon_{\mathbf{k}}$ , measured with respect to the chemical potential, and spin  $\sigma$ , while  $d_{a\sigma}^\dagger$  is the creation operator at the impurity site  $a = 1, 2$  with spin  $\sigma$ ,  $n_a = \sum_{\sigma} d_{a\sigma}^\dagger d_{a\sigma}$  being the occupation number. This model describes two Anderson impurities, each hybridized with its own conduction bath and in turn coupled to the other impurity by a single-particle hopping  $t_{\perp}$ . Since within cluster DMFT the self-consistent baths must mimic the effects of the rest of the lattice on the two sites of the dimer, also the two baths are coupled by a hybridization  $t_{\perp\mathbf{k}}$ . The role of the inter-bath hybridization is to generate a frequency-dependent contribution to the inter-impurity hopping that, together with  $t_{\perp}$ , produce off-diagonal elements  $a \neq b$  to the impurity Green function

$$\mathcal{G}_{ab}(\tau) = -\langle T_{\tau} (d_{a\sigma}(\tau) d_{b\sigma}^\dagger) \rangle.$$

In fact, any coupling among the baths transfers into a coupling among the impurities and vice versa, apart from the frequency dependence that can be anyway neglected in the asymptotic low frequency regime. For this reason, in what follows we will indifferently refer to inter-bath or to inter-site depending upon the context.

Close to the Mott transition the effective impurity model resides well inside the Kondo regime, where  $U \gg V_{\mathbf{k}}, t_{\perp}$ . Here, the model can be mapped via a Schrieffer–Wolff transformation onto two spin-1/2 impurities that, up to order  $1/U$ , are coupled to the two

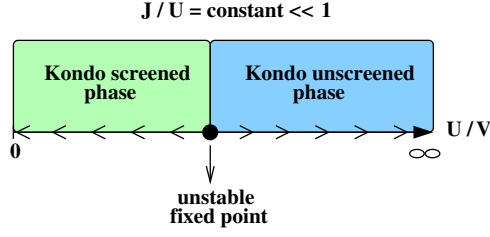


**Figure 4.** Phase diagram of the dimer model (3) as function of  $U/\Gamma$  at fixed  $J/U \ll 1$ .

conduction baths by a Kondo exchange

$$J_K = \frac{8}{U} \sum_{\mathbf{k}} |V_{\mathbf{k}}|^2 \delta(\epsilon_{\mathbf{k}}) \quad (2)$$

and together by an antiferromagnetic  $J = 4t_{\perp}^2/U$ . This means that the spectral distribution of the inter-impurity hybridization

$$\sum_{\sigma} \langle (d_{1\sigma}^{\dagger} d_{2\sigma} + \text{H.c.}) \rangle = -4 \int_{-\infty}^0 \frac{d\omega}{\pi} \text{Im } \mathcal{G}_{12}(\omega),$$

is transferred to high energy, and what remains at low energy is mainly the exchange  $J$ . Within the DMFT self-consistency scheme, we should then expect that also the direct hybridization among the baths,  $t_{\perp\mathbf{k}}$ , behaves similarly, which suggests that one could start the analysis with the large  $U$  limit of the Hamiltonian

$$\begin{aligned} \mathcal{H} &= \sum_{a=1}^2 \left[ \sum_{\mathbf{k}\sigma} \epsilon_{\mathbf{k}} c_{a\mathbf{k}\sigma}^{\dagger} c_{a\mathbf{k}\sigma} - \left( V_{\mathbf{k}} c_{a\mathbf{k}\sigma}^{\dagger} d_{a\sigma} + \text{H.c.} \right) \right] + \frac{U}{2} \sum_{a=1}^2 (n_a - 1)^2 + J \mathbf{S}_1 \cdot \mathbf{S}_2 \\ &\equiv \sum_{a=1}^2 \mathcal{H}_a^K + J \mathbf{S}_1 \cdot \mathbf{S}_2, \end{aligned} \quad (3)$$

where  $\mathbf{S}_a$  is the spin density operator of impurity  $a = 1, 2$ , plus a weak inter-bath hybridization to be considered as a perturbation. This does not at all imply that the latter is irrelevant. Rather, as we are going to discuss, this hybridization turns out to be a relevant perturbation. It only means that this perturbation becomes influential at energy scales much smaller than those at which the main effects caused by the competition between  $J$  and  $J_K$  start to appear, as we shall discuss later. For the time being, let us consider the Hamiltonian (3). This model was originally studied with NRG by Jones and Varma [8–10]. They found that the phase diagram includes two stable phases. When the Kondo temperature,  $T_K$ , is much larger than  $J$ , each impurity is Kondo screened by its conduction bath. On the contrary, when  $J \gg T_K$ , the two impurities lock into a singlet and no Kondo screening is required anymore. These two stable phases were found to be separated by a critical point with non-Fermi liquid properties [10]. We notice that, since  $T_K$  is a decreasing function of  $U$ , the phase diagram at fixed  $J/U \ll 1$  as a function of  $U/\Gamma$ , where  $\Gamma = \Gamma(0)$  is the hybridization width defined through

$$\Gamma(\epsilon) = \pi \sum_{\mathbf{k}} V_{\mathbf{k}}^2 \delta(\epsilon - \epsilon_{\mathbf{k}}), \quad (4)$$

also includes a critical point at some  $(U/\Gamma)_*$ , see figure 4. More specifically, since the Kondo temperature in units of half the conduction bandwidth behaves, at  $J = 0$  and for large  $U$ , as [4]

$$T_K \sim \sqrt{\frac{8\Gamma}{\pi U}} e^{-\pi U/8\Gamma}, \quad (5)$$

one expects the critical point to occur approximately around

$$\frac{U}{\Gamma} \sim \frac{8}{\pi} \ln \frac{1}{J}. \tag{6}$$

In other words, perturbation theory breaks down at a finite value of the interaction within model (3), which is *per se* an interesting situation uncommon in interacting Fermi systems.

The detailed properties of the critical point were later unraveled in [11, 12] by means of conformal field theory (CFT). The use of CFT to study impurity models relies on the fact that only a finite number of conduction electron scattering channels are hybridized with the impurity. This implies that, when  $\Gamma(\epsilon)$ , equation (4), is smooth around the chemical potential,  $\epsilon = 0$ , on a scale larger than the Kondo temperature, the asymptotic low temperature/frequency behavior is similar to a conventional one-dimensional semi-infinite chain of non-interacting electrons, the impurity sitting at the edge. It is known that non-interacting electrons in one dimension can be mapped through bosonization [35] onto a 1 + 1 critical field theory—the criticality corresponding to the fermionic spectrum being gapless—that is not only scale but also conformal invariant. This allows to fully identify and classify all critical properties: thermodynamic quantities, correlation functions and finite size energy spectra [36–38, 30]. In impurity models, the effective one-dimensional chain turns out to be semi-infinite, implying that one has actually to deal with a boundary CFT [39]. Since a single impurity cannot induce any gap in the bulk spectrum, the conformal invariance of the free electrons remains intact; the only effect of the impurity is to change the boundary conditions (BCs) among the conformally invariant ones. A crucial step to determine the allowed BCs is the so-called *conformal embedding* [30], which amounts to identifying the conformal field theories corresponding to the symmetry groups under which the Hamiltonian of the conduction electrons plus the impurity stays invariant. Note that the number of gapless degrees of freedom must be conserved, which corresponds, within CFT, to the fact that the CFTs in the absence and presence of the impurity have the same total *central charge* [30]. A conformal embedding can be justified rigorously by identifying the partition function of free electrons with that obtained by combining the partition functions of the CFTs that emerge out of the embedding. Some simple applications of this very powerful method are given in the appendix. In the most favorable cases, the proper BCs correspond to conformally invariant BCs only within one of the different CFTs of the embedding. The next useful information is that the conformally invariant BCs within each sector can be obtained by the so-called *fusion hypothesis* [39, 40], according to which, starting from the spectrum of a known BC, one can obtain all the others upon *fusion* with the proper scaling fields, called *primary fields*, of the CFT, see the appendix. *Fusion* is just the technical word to denote the process in which the impurity with its quantum numbers dissolves into the conduction electron Fermi sea.

Let us consider for instance model (3), and assume, for simplicity, that the two baths are particle–hole invariant. As a consequence, the baths, in the absence of the impurities, can be described by a CFT [40] which includes independent spin  $SU(2)_1$  and charge isospin  $SU(2)_1$  for each bath, see appendix, namely an overall

$$\left( SU(2)_1^{(1)} \times SU(2)_1^{(2)} \right)_{\text{charge}} \times \left( SU(2)_1^{(1)} \times SU(2)_1^{(2)} \right)_{\text{spin}}.$$

The subscript in  $SU(2)_k^{(a)}$  can be regarded here as the number of copies of spin-1/2 or isospin-1/2 electrons participating to the  $SU(2)$  algebra [35], while the superscript refers to the bath. Since the charge isospin generators commute with the Hamiltonian even when the coupling to the impurities is switched on, the charge sector can still be represented by two independent isospin  $SU(2)_1$  CFTs. On the other hand, only the total spin  $SU(2)$  transformations leave the

Hamiltonian invariant, which translates into an  $SU(2)_2$  (two copies of electrons) CFT. As a result the proper embedding in the spin sector is [11], see also the appendix,

$$\left( SU(2)_1^{(1)} \times SU(2)_1^{(2)} \right)_{\text{spin}} \rightarrow SU(2)_2 \times Z_2,$$

where  $Z_2$  denotes an Ising CFT which reflects the symmetry under permutation of the two baths. The Ising CFT has three primary fields, the identity  $I$ , with dimension 0,  $\epsilon$  (the thermal operator), with dimension 1/2, and  $\sigma$  (the Ising order parameter), with dimension 1/16. Each state and operator can then be identified by the quantum numbers  $(I_1, I_2, S, \text{Ising})$  where  $I_1$  and  $I_2$  refer to the charge isospin of each channel,  $S$  to the total spin and Ising to the  $Z_2$  sector.

Affleck and Ludwig [11, 12] realized that the different fixed points found by NRG, see figure 4, correspond to the three different BCs of the Ising CFT, namely two fixed BCs, the stable phases—where one Ising spin orientation is prohibited at the boundary—and one free BC, the unstable fixed point—where both orientations are allowed. Starting from the unscreened phase, the Kondo screened phase is obtained by fusion with the Ising primary field  $\epsilon$ , while the unstable critical point is obtained by fusion with the Ising order parameter  $\sigma$ . Furthermore, the critical point is identified by a finite residual entropy  $S(T = 0) = \frac{1}{2} \ln 2$ , showing that part of the impurity degrees of freedom remains unscreened.

CFT also determines, by the so-called double fusion [40], the dimensions of the relevant operators, see the appendix. It turns out that there are three equally relevant (i.e. with dimension less than 1) symmetry breaking perturbations which can destabilize the unstable fixed point, identified by two asterisks in table A.4 of the appendix. They all have the same dimension 1/2 as the invariant operator, single asterisk in table A.4 of the appendix, which moves away from the fixed point and corresponds to a deviation of  $J$  from its fixed point value  $J_*$  at fixed  $T_K$ , or, vice versa, a deviation of  $T_K$  at fixed  $J$ . The first symmetry breaking operator is an opposite spin magnetization for the two baths, namely a local operator of the form

$$h_{\text{AF}} (\mathbf{S}_1 - \mathbf{S}_2), \quad (7)$$

and corresponds in table A.4 of the appendix to the operator with quantum numbers  $(I_1, I_2, S, \text{Ising}) = (0, 0, 1, 0)$ . The second is a BCS term in the inter-bath Cooper singlet channel:

$$h_{\text{SC}} \left( d_{1\uparrow}^\dagger d_{2\downarrow}^\dagger + d_{2\uparrow}^\dagger d_{1\downarrow}^\dagger \right) + \text{H.c.} \quad (8)$$

The last perturbation is a direct hybridization between the two baths,

$$\sum_{\sigma} h_{\perp} d_{1\sigma}^\dagger d_{2\sigma} + \text{H.c.}, \quad (9)$$

which breaks the  $O(2)$  channel symmetry. Both (8) and (9) correspond in table A.4 of the appendix to the spin singlet operator with quantum numbers  $(I_1, I_2, S, \text{Ising}) = (1/2, 1/2, 0, 0)$ . On the contrary, both a chemical potential shift that moves away from particle hole symmetry, or a perturbation that splits the two conduction channels, do not destabilize the critical point. Indeed, if the position of the impurity levels is modified, so that the average number of electrons on each impurity moves away from  $\langle n_a \rangle = 1$ ,  $a = 1, 2$ , the critical point is still encountered, although it will shift to larger  $U/\Gamma$  at fixed  $J/U \ll 1$  [34], see figure 5.

### 2.1. Dynamical behavior of the impurity dimer

The instability channel (9) is very important since, as we mentioned, the inter-bath as well as the inter-impurity hybridization are always present. Therefore the relevant issue becomes whether this hybridization completely washes out the critical behavior of the underneath critical point, or whether a critical region still remains. In order to answer this question, it is convenient

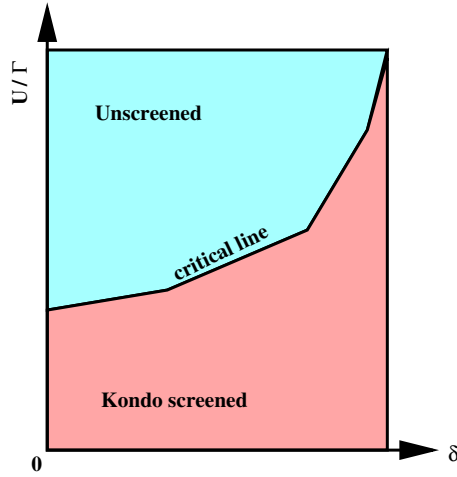


**Figure 5.** Phase diagram of (3) as function of  $U/\Gamma$  and  $\delta = |\langle n \rangle - 1|$ ,  $\langle n \rangle$  being the average occupancy of each impurity, at fixed  $J/U \ll 1$ .

to analyze the impurity spectral function, which is also the key ingredient of the DMFT self-consistency procedure.

We start by noticing that, in spite of the fact that both Kondo screened and unscreened phases of the Hamiltonian (3) are Fermi liquid-like in Nozières’ sense [41] (namely they correspond asymptotically to well defined limits of free electron scattering off a structureless impurity potential, infinite in the Kondo screened phase and zero in the unscreened one), the dynamical properties of the impurities are completely different. Indeed, the conduction electron scattering  $S$ -matrix at the chemical potential should satisfy

$$S = 1 - 2 \frac{\rho(0)}{\rho_0}, \tag{10}$$

where  $\rho(0)$  is the actual density of states (DOS) of the impurity at the chemical potential, while  $\rho_0 = 1/(\pi\Gamma)$  is its non-interacting  $U = J = 0$  value. Since both stable phases are Fermi liquid-like, it follows that the  $S$  matrix is unitary, hence can be written as  $S = e^{2i\delta}$ , where  $\delta$  is the phase shift at the chemical potential. The Kondo screened phase is identified by a phase shift  $\delta = \pi/2$ , that implies  $S = -1$  hence  $\rho(0) = \rho_0$ ; the DOS at the chemical potential is unaffected by the interaction. On the contrary, in the unscreened phase  $\delta = 0$ , thus  $S = 1$  and  $\rho(0) = 0$ . In other words, while in the Kondo screened phase the DOS is peaked at the chemical potential—the conventional Kondo resonance behavior—it vanishes in the unscreened one. Furthermore, according to CFT, right at the critical point  $S = 0$ , namely  $\rho(0) = \rho_0/2$ . These results are actually reproduced by NRG, see e.g. [34]. In figure 6, we draw our NRG results for the impurity DOS of the dimer model (3) for  $U = 8$ ,  $J = 0.00125$ , in units of half the conduction bandwidth, and for various values of  $\Gamma$  across the critical point  $\Gamma_*$ , which lies between 0.42 and 0.44. The upper inset shows that, on large scales, the DOSs in the screened and unscreened phases are practically indistinguishable. The differences emerge at very low energies. Apart from the value of the DOS at the chemical potential, which, as mentioned, can be anticipated by general scattering theory arguments, other useful information can be extracted from the whole low energy behavior. As was realized in [34], the DOS is controlled by two energy scales. In the Kondo screened phase, there is a narrow Kondo peak on top of a broad resonance. The Kondo peak shrinks as the critical point is approached, while

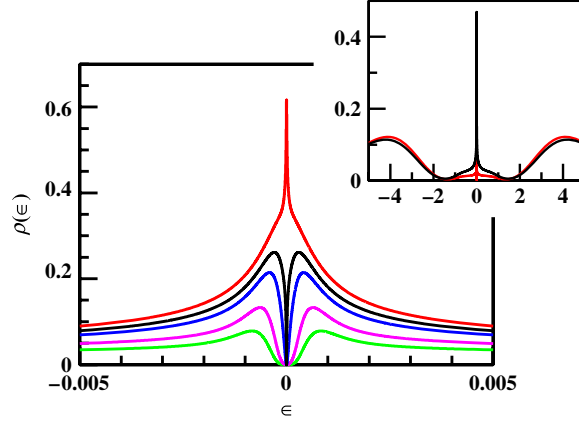


**Figure 6.** Main panel: low energy behavior of the impurity DOS of the dimer model (3) with  $U = 8$ ,  $J = 0.00125$  and, from top to bottom,  $\Gamma = 0.44, 0.42, 0.4, 0.35, 0.3$ , in units of half the conduction bandwidth. We observe that the rough estimate of the order of magnitude of the critical  $U/\Gamma \sim -(8/\pi) \ln J \simeq 17.3$ , see equation (6), agrees with the actual numerical value  $(U/\Gamma)_* \sim 18.2$ . Upper inset: the DOS behavior in the whole energy range with the same  $U$  and  $J$  and with  $\Gamma = 0.6$ , top curve, and  $\Gamma = 0.3$ . The Hubbard bands are clearly visible, while the low energy parts are hardly distinguishable. The discretization parameter [28, 29] that we used is  $\Lambda = 2$ .

the width of the large resonance remains practically constant. Indeed, right at the critical point, only the latter survives. On the contrary, inside the unscreened phase, the Kondo peak turns into a narrow pseudo-gap within the broad resonance, leading to a low energy DOS  $\rho(\epsilon) \sim \epsilon^2$ . This behavior has been found to be well reproduced by the following model DOS at low energy [34]:

$$\rho_{\pm}(\epsilon) = \frac{\rho_0}{2} \left( \frac{T_+^2}{\epsilon^2 + T_+^2} \pm \frac{T_-^2}{\epsilon^2 + T_-^2} \right), \quad (11)$$

where the + sign refers to the screened phase and the – one to the unscreened.  $T_+$  is the width of the broad resonance,  $T_-$  the one of the narrow peak in the screened phase and the amplitude of the pseudo-gap in the unscreened regime. As the critical point is approached on both sides,  $T_- \sim |\Gamma - \Gamma_*|^2 \rightarrow 0$  [34], in accordance with the CFT prediction that the relevant operator has dimension 1/2. Away from particle–hole symmetry,  $\langle n_a \rangle \neq 1$ , the two stable phases are still identified by a relative  $\pi/2$  shift of  $\delta$ , although the unscreened phase value,  $\delta_0$ , is different from zero. In this case, the following model DOS was found to reproduce well the NRG data [34]:

$$\rho_{\pm}(\epsilon) = \frac{\rho_0}{2} \left[ \frac{T_+^2 + \mu_{\pm}^2}{(\epsilon + \mu_{\pm})^2 + T_+^2} \pm \cos 2\delta_0 \frac{T_-^2}{\epsilon^2 + T_-^2} \right], \quad (12)$$

with  $\mu_{\pm} = \pm T_+ \sin 2\delta_0$ . This formula shows that, in the unscreened phase, the pseudo-gap remains pinned at the chemical potential, even if, since the broad resonance shifts, the pseudo-gap fills in of an amount proportional to the ‘doping’, i.e.  $|\langle n_a \rangle - 1|$ .

By the model DOS (11), one can extract a model self-energy,  $\Sigma(i\omega)$  in Matsubara frequencies, which, for low  $\omega > 0$ , behaves as

$$\Sigma_+(i\omega) \simeq -i\omega \left( \frac{\Gamma(T_+ + T_-)}{2T_+T_-} - 1 \right) + i\omega^2 \frac{\Gamma(T_+ - T_-)^2}{4T_+^2T_-^2}, \quad (13)$$

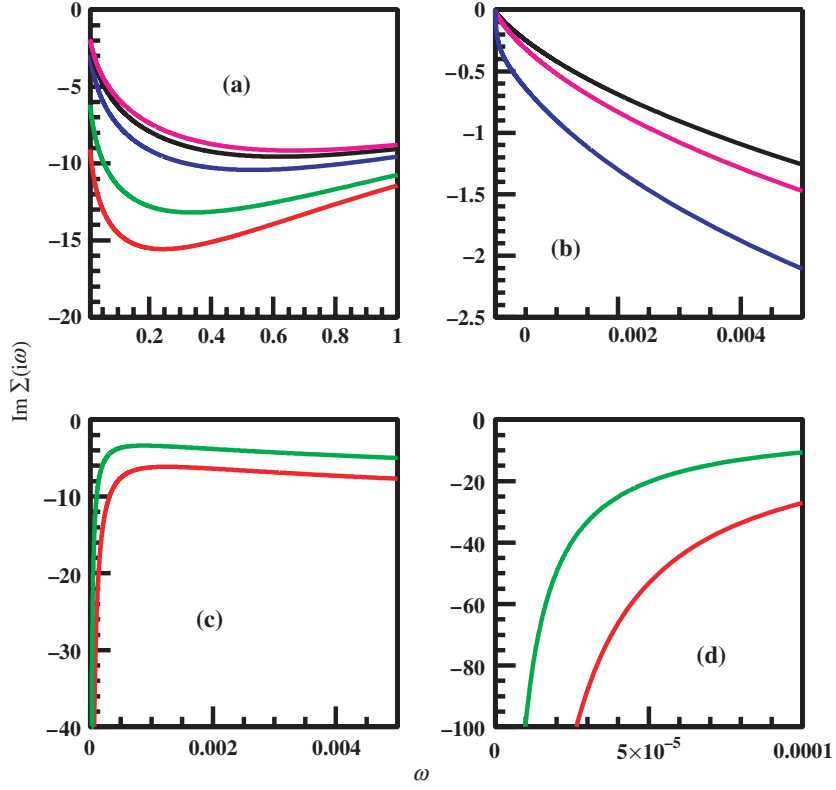


**Figure 7.** Imaginary part of  $\Sigma(i\omega)$  versus  $\omega$  for  $U = 8$  and  $J = 0.00125$ : (a) whole frequency range behavior for  $\Gamma = 0.5, 0.48, 0.44, 0.35, 0.3$ , from top to bottom; (b) low frequency behavior for the Kondo screened values  $\Gamma = 0.5, 0.48, 0.44$ ; (c) and (d) low frequency behavior for the unscreened values  $\Gamma = 0.35, 0.3$ . These results were obtained with  $\Lambda = 2$ .

in the Kondo screened phase, as

$$\Sigma_{-}(i\omega) \simeq -i\frac{1}{\omega} \frac{2\Gamma T_{+} T_{-}}{T_{+} - T_{-}} - i\Gamma \frac{T_{+} + 3T_{-}}{T_{+} - T_{-}} - i\omega \frac{2\Gamma - T_{+} + T_{-}}{T_{+} - T_{-}}, \quad (14)$$

in the unscreened one, and finally as

$$\Sigma_{*}(i\omega) \simeq -i\Gamma - i\omega \frac{2\Gamma - T_{+}}{T_{+}}, \quad (15)$$

exactly at the critical point,  $T_{-} = 0$ , or in the range  $T_{-} \ll \omega \ll T_{+}$ . The model self-energy reproduces well the actual NRG results, shown in figure 7. Only in the screened phase, panels (a) and (b) in figure 7, the self-energy has the standard perturbative behavior,  $\Sigma(i\omega) \sim (1 - 1/Z) i\omega$ , with  $Z$  the quasiparticle residue, which breaks down at the critical point, where  $\Sigma(i\omega)$  goes to a constant value for  $\omega \rightarrow 0$ , and even more in the unscreened regime where, as shown on different frequency ranges in panels (a), (c) and (d) of figure 7,  $\Sigma(i\omega)$  diverges as  $\omega \rightarrow 0$ .

Let us now consider the original dimer model (1). In order not to deal with too many Hamiltonian parameters, we consider the case in which the inter-bath hybridization is zero,  $t_{\perp \mathbf{k}} = 0$ , and take  $U = 8$ , as before, and  $t_{\perp} = 0.05$ , such that  $J = 4t_{\perp}^2/U = 0.00125$ , the

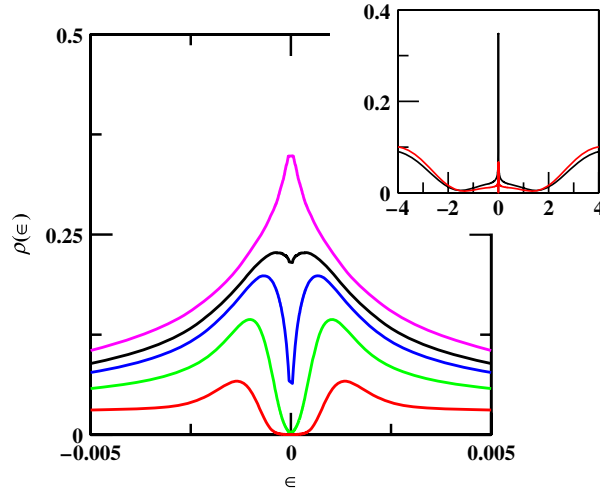


**Figure 8.** Main panel: low energy behavior of the impurity DOS of the model (1) with  $U = 8$ ,  $t_{\perp} = 0.05$  and, from top to bottom,  $\Gamma = 0.5, 0.47, 0.45, 0.4, 0.3$ , in units of half the conduction bandwidth. Upper inset: the DOS behavior in the whole energy range with the same  $U$  and  $J$  and with  $\Gamma = 0.5$ , top curve, and  $\Gamma = 0.2$ . These results were obtained with  $\Lambda = 2$ .

same value used previously. In this model  $t_{\perp}$  has a double role: on one side it generates a spin exchange able to drive the model across the critical point, but at the same time it also breaks the relevant  $O(2)$  channel symmetry thus making the critical point inaccessible. Indeed, as shown by the behavior of the impurity DOS in figure 8, a crossover now joins the Kondo screened phase and the unscreened one. There are still quite distinct DOSs deep inside the screened and unscreened phases, the former characterized by a Kondo resonance, the latter by a pseudo-gap. However, the transition from the two limiting behaviors is now just a crossover, although quite sharp.

More interesting are the changes that intervene in the impurity self-energy with respect to the model (3). In presence of  $t_{\perp}$ , the self-energy, besides diagonal elements,  $\Sigma_{11}(i\omega) = \Sigma_{22}(i\omega)$ , which are imaginary, also acquires off-diagonal components,  $\Sigma_{12}(i\omega) = \Sigma_{21}(i\omega)^*$ , which turn out to be purely real. In figure 9, we plot  $\text{Im} \Sigma_{11}(i\omega)$  and  $\text{Re} \Sigma_{12}(i\omega)$  versus  $\omega$  for the same values of  $\Gamma$ 's as in figure 8, on two different energy ranges. We notice that the gross features of  $\Sigma_{11}(i\omega)$  remain intact, namely, as the model moves from the screened regime towards the unscreened one, the diagonal self-energy increases quite fast in absolute value. However, a linearly vanishing 'Fermi liquid' behavior is eventually recovered at very low energies, as shown in the left bottom panel of figure 9. In fact, the model in the presence of  $t_{\perp}$  does not need to develop a singular self-energy anymore to open up a pseudo-gap at the chemical potential as in model (3). It is the off-diagonal self-energy,  $\Sigma_{12}$ , that accomplishes the job in this case. Indeed, as shown in the right panels of figure 9,  $\Sigma_{12}$  becomes so large at low energy to open up an appreciable hybridization gap, not explainable by the tiny value of  $t_{\perp}$  as compared to the hybridization width  $\Gamma$ . This result could be justified simply by stating that the strong repulsion  $U$  enhances the effective strength of  $t_{\perp}$ . However, the previous results on the dimer model (3) and the strong energy dependence of the self-energy, see figure 9, suggest that this anomalous behavior reflects rather the properties of the avoided critical point which exists in the presence of  $J$  at  $t_{\perp} = 0$ . In other words, we believe that our results testify that a sizable critical region still exists and largely explains the physical behavior.

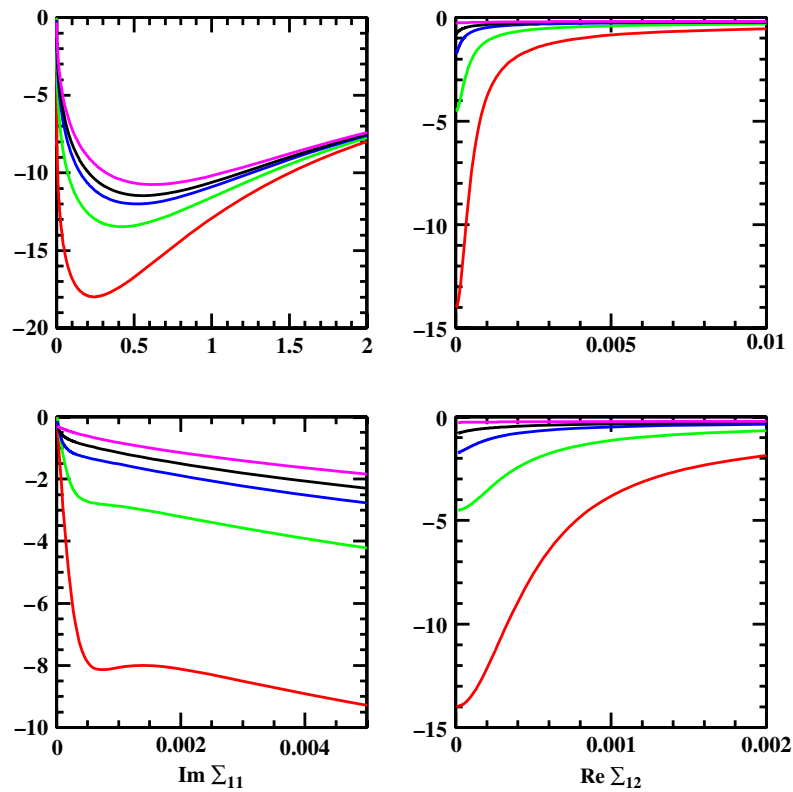


**Figure 9.** y-axis: imaginary part of  $\Sigma_{11}(i\omega)$ , left panels, and real part of  $\Sigma_{12}(i\omega)$ , right panels, versus  $\omega$  (x-axis) for  $U = 8$ ,  $t_{\perp} = 0.05$  and, from top to bottom,  $\Gamma = 0.5, 0.47, 0.45, 0.4, 0.3$  and  $\Lambda = 2$ . In the top figures the whole frequency range is showed, while in the bottom ones only the very low frequency behavior.

Obviously, as in any other case of avoided criticality, the width of the critical region depends on the actual value of  $t_{\perp}$  with respect to the other parameters  $U$  and  $\Gamma$ . Since both  $t_{\perp}$  and  $\Gamma$  are self-consistently determined within DMFT as function of  $U$  and the bare bandwidth, we cannot establish with certainty what might happen in a DMFT simulation of a Hubbard model using a dimer as a representative cluster. However, because the exchange  $J$  derives from high energy processes and survives even inside the Mott insulator, while the coherent hopping dies out at the Mott transition, we believe that a sizable critical region should exist in the effective impurity cluster model and plays an influential role in determining the bulk properties after the DMFT self-consistency.

### 3. The impurity trimer

An important lesson of the impurity dimer was that, in order to identify in all details the properties of the critical region, it is more convenient to study a model in which the impurities are coupled together by an antiferromagnetic exchange rather than by a hopping as would be the case in reality. In the end, we will discover that, just like in the dimer example, the hopping is a relevant perturbation, and yet a critical region survives. Therefore, let us consider the next simple cluster, which is the impurity trimer drawn in figure 10 with the Hamiltonian

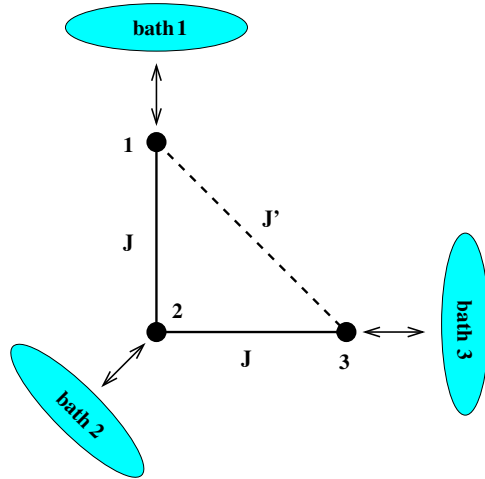


Figure 10. The impurity trimer with the Hamiltonian (16).

$$\mathcal{H} = \sum_{a=1}^3 \mathcal{H}_a^K + J (\mathbf{S}_1 + \mathbf{S}_3) \cdot \mathbf{S}_2 + J' \mathbf{S}_1 \cdot \mathbf{S}_3, \tag{16}$$

where  $\mathcal{H}_a^K$  has been defined in (3). This model describes three spin-1/2 impurities, coupled together by antiferromagnetic  $J$  and  $J'$  and each of them hybridized to a conduction bath. As before, we assume that the baths are degenerate and particle-hole invariant. This model, although simplified by the absence of any inter-impurity hopping, is much more complicated than the dimer model (3). Therefore, in order to unravel its phase diagram, we need to combine the NRG analysis, which provides the low energy spectra of the various fixed points, with CFT, which allows to identify each fixed point with a particular boundary CFT, whose properties can be determined exactly. For this reason, we cannot start our analysis before introducing some CFT preliminaries.

### 3.1. CFT preliminaries for the trimer

As in the dimer example, also in the trimer model (16) at particle-hole symmetry the charge degrees of freedom can be described by three independent isospin  $SU(2)_1^{(a)}$  CFTs,  $a = 1, 2, 3$ . For the spin degrees of freedom, the expression of the inter-impurity exchange suggests naturally that we must first couple the spin sectors of baths 1 and 3 into an overall  $SU(2)_2$  via the embedding

$$SU(2)_1^{(1)} \times SU(2)_1^{(3)} \rightarrow SU(2)_2^{(1-3)} \times Z_2, \tag{17}$$

and finally couple the  $SU(2)_2$  to the bath 2 into an  $SU(2)_3$ , according to

$$SU(2)_2^{(1-3)} \times SU(2)_1^{(2)} \rightarrow SU(2)_3 \times (\text{TIM}), \tag{18}$$

where TIM stands for the tricritical Ising model CFT with central charge  $c = 7/10$ . It describes for instance the tricritical point of the two-dimensional Blume-Capel model which involves an Ising spin variable and a vacancy variable indicating if the site is empty or occupied [42, 43]. The above conformal embedding can be rigorously justified by the *character decomposition* [30], although we do not give here the details of this lengthy and involved construction.

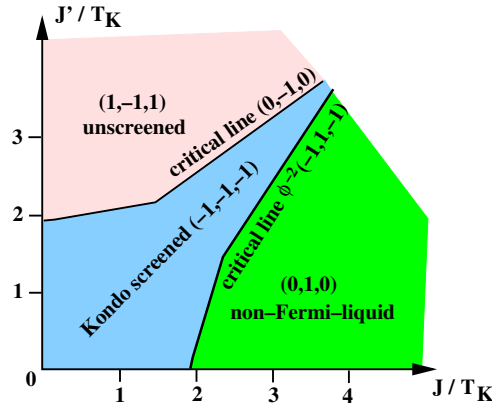


**Figure 11.** Phase diagram of the trimer model (16). All different phases are discussed in the text, and their properties briefly summarized in table 1.

The primary fields of an  $SU(2)_k$  as well as of the Ising CFTs, together with their fusion, i.e. multiplicative, rules, are discussed in the appendix. For what concerns the TIM, it contains six primary fields, the identity  $I$ , with dimension 0, the thermal energy operator  $\epsilon$ , with dimension  $1/10$ , the energy density of annealed vacancies  $t$ , with dimension  $3/5$ ,  $\epsilon''$ , with dimension  $3/2$ , the magnetization  $\sigma$ , with dimension  $3/80$ , and the subleading magnetization operator  $\sigma'$ , with dimension  $7/16$  [30]. Their fusion rules can be found for instance in [30, p 224].

As we previously mentioned, the possible conformally invariant boundary conditions can be classified by means of the fusion hypothesis [15, 16, 12]. Namely, starting from the spectrum of a simple BC, one can obtain the spectra of other allowed BCs upon fusion with primary fields of the CFTs. By comparing the low energy spectra determined in this way with those obtained by NRG, one can identify and characterize all fixed points of the model.

### 3.2. Fixed points in the trimer phase diagram

In figure 11, we draw the phase diagram of the trimer as obtained by NRG [27–29]. In order to have a classification scheme which works equally well for Fermi liquid and non-Fermi liquid phases, the fixed points are identified through the zero-frequency values of the scattering  $S$ -matrices of the baths,  $(S_1, S_2, S_3)$ , which can be obtained by CFT [44, 45] through the modular  $S$ -matrix [30]. Note that, through equation (10), the values of the scattering  $S$ -matrices give direct access to the values of the DOS at the chemical potential of each impurity. We just recall that  $S_a = -1$  means that the impurity  $a$  DOS has a Kondo resonance,  $S_a = 1$  that it has a pseudo-gap,  $\rho_a(\epsilon) \sim \epsilon^2$ , while any intermediate value implies a non-Fermi liquid behavior. The physical properties of the different phases are furthermore summarized in table 1.

Let us now present briefly the features of each fixed point.

3.2.1.  $(S_1, S_2, S_3) = (-1, -1, -1)$ . This fixed point, that describes a conventional perfectly Kondo screened phase, will be used as the ancestor BC which, upon fusion with primary fields, will provide all other BCs. It is quite obvious that this phase exists and extends in a whole region around the origin  $J = J' = 0$  in figure 11. Indeed, when  $J = J' = 0$ , each impurity is independently Kondo screened by its own conduction bath and this perfect screening cannot be affected by finite  $J$  and  $J'$  much smaller than the Kondo temperature. It is far less obvious

**Table 1.** Summary of the main physical properties of the different phases in figure 11, including the behavior of the zero-frequency DOSs for the three impurities,  $\rho_i(0)$  with  $i = 1, 2, 3$ , with respect to the non-interacting value  $\rho_0$ , and the dimension of the relevant symmetry breaking single-particle operators. ‘NOT’ means that the operator is not relevant, i.e. has dimension not smaller than 1.  $\phi$  is the golden ratio.

	(0, 1, 0)	$\phi^{-2}(-1, 1, -1)$	(-1, -1, -1)	(0, -1, 0)	(1, -1, 1)
$\rho_1(0)/\rho_0 = \rho_3(0)/\rho_0$	1/2	$(1 + \phi^{-2})/2$	1	1/2	0
$\rho_2(0)/\rho_0$	0	$(1 - \phi^{-2})/2$	1	1	1
$\mathbf{S}_1 + \mathbf{S}_3 - 2\mathbf{S}_2$	1/2	2/5	NOT	NOT	NOT
$\mathbf{S}_1 - \mathbf{S}_3$	NOT	NOT	NOT	1/2	NOT
$d_1^\dagger d_3^a$	1/2	3/5	NOT	1/2	NOT
$d_1^\dagger d_3^{\dagger a}$	1/2	3/5	NOT	1/2	NOT
$(d_1^\dagger + d_3^\dagger) d_2^a$	NOT <sup>b</sup>	3/5	NOT	NOT <sup>b</sup>	NOT
$(d_1^\dagger + d_3^\dagger) d_2^{\dagger a}$	NOT <sup>b</sup>	3/5	NOT	NOT <sup>b</sup>	NOT

<sup>a</sup> These particle–hole and particle–particle operators are spin singlets.

<sup>b</sup> These operators are not relevant in the sense that their dimension is not smaller than 1. However, they do generate in perturbation theory one of the truly relevant perturbations, with dimension smaller than 1, so that in reality they are relevant too.

that this fixed point remains stable for large  $J \simeq J'$ . When  $J' = J \gg T_K$ , the impurities lock into two degenerate  $S = 1/2$  configurations. In the first, sites 1 and 3 are coupled into a triplet which in turn is coupled with site 2 into an overall spin-1/2 configuration. Since this is even by interchanging 1 with 3, we denote it as  $|e\rangle$ . The other configuration, which we denote as  $|o\rangle$  as it is odd under  $1 \leftrightarrow 3$ , corresponds to sites 1 and 3 coupled into a singlet, leaving behind the free spin-1/2 moment of site 2. The Kondo exchange projected onto this subspace reads

$$\begin{aligned} & \frac{J_K}{3} |e\rangle\langle e| \mathbf{S} \cdot (2\mathbf{J}_1(0) - \mathbf{J}_2(0) + 2\mathbf{J}_3(0)) + J_K |o\rangle\langle o| \mathbf{S} \cdot \mathbf{J}_2(0) \\ & - \frac{J_K}{\sqrt{3}} (|e\rangle\langle o| + |o\rangle\langle e|) \mathbf{S} \cdot (\mathbf{J}_1(0) - \mathbf{J}_3(0)), \end{aligned} \quad (19)$$

where  $\mathbf{S}$  describes the effective  $S = 1/2$  of the trimer, while  $\mathbf{J}_a(0)$  is the spin density of bath  $a = 1, 2, 3$  at the impurity site, assumed to be the origin. All the above screening channels flow to strong coupling within a simple one-loop calculation. Since it can be readily shown that the impurity can be perfectly screened, both in the spin and in the even–odd channels, one has to conclude that the whole line  $J = J'$  at finite  $J_K$  corresponds to the Kondo screened fixed point  $(-1, -1, -1)$ , as in figure 11. A small deviation from  $J = J'$  is an irrelevant perturbation that splits the degeneracy between  $|e\rangle$  and  $|o\rangle$ . Only a finite deviation eventually destabilizes this fixed point, the faster the smaller  $J_K$ .

3.2.2.  $(S_1, S_2, S_3) = (0, 1, 0)$ . This fixed point occurs for  $J \gg T_K, J'$ , see figure 11. The NRG spectrum is compatible with that obtained by fusing the  $(-1, -1, -1)$  fixed point with the field  $\sigma'$  of the TIM. It is not difficult to realize that this fixed point is equivalent to the non-Fermi liquid phase of the  $S = 1/2$  two-channel Kondo model [15, 16]. Indeed if  $J' = 0$  and  $J$  is large, the trimer locks into the  $S = 1/2$  configuration which we previously denoted as  $|e\rangle$ , to indicate the even parity upon  $1 \leftrightarrow 3$ . The Kondo exchange projected onto this configuration is,

see equation (19),

$$\mathbf{S} \cdot \sum_{a=1}^3 J_K^{(a)} \mathbf{J}_a(0) = \frac{J_K}{3} \mathbf{S} \cdot (2\mathbf{J}_1(0) - \mathbf{J}_2(0) + 2\mathbf{J}_3(0)). \quad (20)$$

Hence, while baths 1 and 3 are still antiferromagnetically coupled, the coupling with bath 2 turns effectively ferromagnetic. The ordinary one-loop renormalization group calculation would predict that the Kondo exchanges  $J_K^{(1)} = J_K^{(3)} > 0$  flow towards strong coupling, while  $J_K^{(2)} < 0$  flows towards zero. This suggests that a model with  $J_K^{(1)} = J_K^{(3)} \gg -J_K^{(2)} > 0$  should behave asymptotically as (20). If  $J_K^{(2)} = 0$  this is just the two-channel spin-1/2 impurity model [15, 16], which is non-Fermi liquid with  $S$ -matrices  $S_1 = S_3 = 0$  [44, 45]. It is easy to show that the small ferromagnetic  $J_K^{(2)}$  transforms into an antiferromagnetic exchange of the form  $\mathbf{J}_2(0) \cdot (\mathbf{J}_1(0) + \mathbf{J}_3(0))$ , which is irrelevant. Consequently, we expect that this phase should remain non-Fermi liquid and identified by the  $S$ -matrices  $(S_1, S_2, S_3) = (0, 1, 0)$ , as indeed confirmed by CFT. In addition, through the modular  $S$ -matrix, one can show that the zero-temperature entropy  $S(0) = 1/2 \ln 2$  is finite and coincides with that of the  $S = 1/2$  two-channel Kondo model. Since  $\sigma' \times \sigma' = I + \epsilon''$ , with the latter having dimension  $3/2 > 1$ , this fixed point is stable to symmetry preserving perturbations. Yet, there are several symmetry breaking relevant perturbations of dimension 1/2. One of them corresponds to the staggered magnetization

$$\mathbf{J}_1 - 2\mathbf{J}_2 + \mathbf{J}_3. \quad (21)$$

All the other relevant operators break the degeneracy between bath 1 and 3, as for instance the spin singlet operator

$$\mathbf{J}_2 \cdot (\mathbf{J}_1 - \mathbf{J}_3), \quad (22)$$

and the direct hopping or singlet pairing between baths 1 and 3, both known to be relevant perturbations at the overscreened non-Fermi liquid fixed point [46]. Note that, although the hopping/pairing operators between baths 1 and 2 as well as 3 and 2 have dimension 1, they do induce indirectly a symmetry breaking coupling among baths 1 and 3 of dimension 1/2, hence they are effectively relevant, specifically marginally relevant. This phase with  $S$ -matrices  $(S_1, S_2, S_3) = (0, 1, 0)$  extends at finite  $J'$  just because  $J'$  does not generate any symmetry breaking relevant perturbation.

The approach to the fixed point is controlled by two leading irrelevant operators of dimension 3/2:  $\epsilon''$  and the scalar product of the staggered magnetization (21) with the first spin descendant. Similarly to the overscreened two-channel Kondo model [15, 16], these operators produce logarithmic singularities in the impurity contribution to the specific heat coefficient and to the magnetic susceptibility,  $C_{\text{imp}}/T \sim \chi_{\text{imp}} \sim \ln(1/T)$ .

3.2.3.  $(S_1, S_2, S_3) = \phi^{-2}(-1, 1, -1)$ . Since the Kondo screened phase,  $(-1, -1, -1)$  and the non-Fermi liquid one,  $(0, 1, 0)$ , are essentially different, it is clear that an unstable critical line separates the two, see figure 11. We find that the NRG spectrum can be reproduced by fusing the  $(-1, -1, -1)$  fixed point with  $\epsilon$  of the TIM. The  $S$ -matrices are  $\phi^{-2}(-1, 1, -1)$  and the residual entropy is  $S(0) = \ln \phi$ , where  $\phi = (1 + \sqrt{5})/2$  is the golden ratio. Since  $\epsilon \times \epsilon = I + t$ , the operator which moves away from the critical line has dimension 3/5. The most relevant symmetry breaking operator is still the staggered magnetization (21), which has now dimension 2/5. Once more, the approach to this fixed point is controlled by the scalar product of the staggered magnetization with the first Kac–Moody descendant of the  $SU(2)_3$  CFT, which has dimension  $1 + 2/5$ . Analogously to the multi-channel Kondo [15, 16], this operator

produces impurity contributions to the specific heat coefficient and magnetic susceptibility that diverge like  $T^{-1/5}$ .

The spin singlet operator (22) is also relevant, although with a larger dimension  $3/5$ . In addition, there is a new class of dimension- $3/5$  operators which correspond to coupling into a spin singlet of two particles, or one hole and one particle, belonging to bath 2 and either bath 1 or 3. Finally, this critical line is stable towards moving away from particle–hole symmetry, as it was the case in the dimer.

**3.2.4.**  $(S_1, S_2, S_3) = (1, -1, 1)$  and  $(S_1, S_2, S_3) = (0, -1, 0)$ . These two fixed points occur when  $J' > J$  is larger or comparable with the Kondo temperature. They have a very simple explanation. Indeed, when  $J = 0$ , site 2 is only coupled to bath 2 with a Kondo exchange, leading to a full screening, i.e.  $S_2 = -1$ . Sites 1 and 3 plus their own baths realize a two-impurity Kondo model which, as discussed before, has two stable regimes. One is Kondo screened,  $S_1 = S_3 = -1$ , for  $J' \ll T_K$ ,  $(S_1, S_2, S_3) = (-1, -1, -1)$  in figure 11, and the other unscreened for  $J' \gg T_K$ ,  $(S_1, S_2, S_3) = (1, -1, 1)$  in figure 11. These two regimes are stable towards switching on a small  $J \ll J'$ . When  $J = 0$ , we also know that an unstable fixed point at  $J' = J'_* \sim T_K$  separates these two stable phases, which is identified by  $S_1 = S_3 = 0$ , hence the label  $(0, -1, 0)$  in figure 11. Since site 2 is tightly bound into a singlet state with bath 2, a finite but small  $J \ll T_K$  will simply generate a ferromagnetic exchange of order  $-J^2/T_K$  by virtually exciting the singlet state. The net effect is that the unstable fixed point at  $J = 0$  is just the end-point of another critical line which, for  $J \ll T_K$ , moves to larger values of  $J'$ . From the CFT viewpoint, the  $(1, -1, 1)$  and  $(0, -1, 0)$  fixed points can be obtained by fusing with  $\epsilon''$  of the TIM or  $\sigma_1$  of the Ising CFT, respectively. The properties of the unstable  $(0, -1, 0)$  critical line are the same as those of the dimer critical point. In particular there is a relevant operator in the singlet Cooper channel that now involves pairing among baths 1 and 3, as well as an equally relevant operator which corresponds to an opposite magnetization of bath 1 and 3, i.e.  $\mathbf{J}_1 - \mathbf{J}_3$ .

### 3.3. Dynamical properties of the trimer

In the  $J$ – $J'$  parameter space of the trimer model (16), the  $J' = 0$  line is actually pertinent to a Hubbard model on a bipartite lattice and with nearest neighbor hopping simulated within cluster DMFT. In this case, the phase diagram is qualitatively similar to that of the dimer model, see figure 5, apart from the fact that the unscreened phase corresponds now to the  $(S_1, S_2, S_3) = (0, 1, 0)$  non-Fermi liquid phase, while the critical line represents the  $(S_1, S_2, S_3) = \phi^{-2}(-1, 1, -1)$  unstable fixed point.

Both the critical line and the non-Fermi liquid phase are unstable to a nearest neighbor hopping. If, instead of three impurities coupled by  $J$ , we consider three impurities coupled by a hopping, the transition from the Kondo screened phase to the non-Fermi liquid one transforms into a crossover between Fermi liquid regimes, exactly like in the dimer. In figure 12, we draw the self-energies in Matsubara frequencies of the three impurities coupled by the spin exchange  $J$  (panels (a) and (b)), as well as of the impurities coupled by a hopping  $t_\perp$  along the bonds 1–2 and 2–3 (panels (c) to (f)). The Hamiltonian parameters are  $U = 8$ ,  $J = 0.00125$  and  $t_\perp = 0.05$ , like in figures 7 and 9, while  $\Gamma = 0.4, 0.44, 0.5$ . In the absence of  $t_\perp$ , the self-energies, which are diagonal and imaginary, behave as  $\text{Im } \Sigma_{aa}(i\omega) \sim -\omega$  in the Kondo screened phase,  $\Gamma = 0.5$ , and tend to a constant at the fixed point,  $\Gamma \simeq 0.44$ . In the unscreened phase,  $\Gamma = 0.4$ ,  $\text{Im } \Sigma_{11}(i\omega) = \text{Im } \Sigma_{33}(i\omega) \rightarrow \text{const.}$  while  $\text{Im } \Sigma_{22}(i\omega) \sim -1/\omega$ , in accordance with the values of the scattering  $S$ -matrices. Similarly to the dimer, when the impurities are instead coupled by a single-particle hopping, a Fermi liquid behavior  $\text{Im } \Sigma_{aa}(i\omega) \sim -\omega$  is eventually recovered at

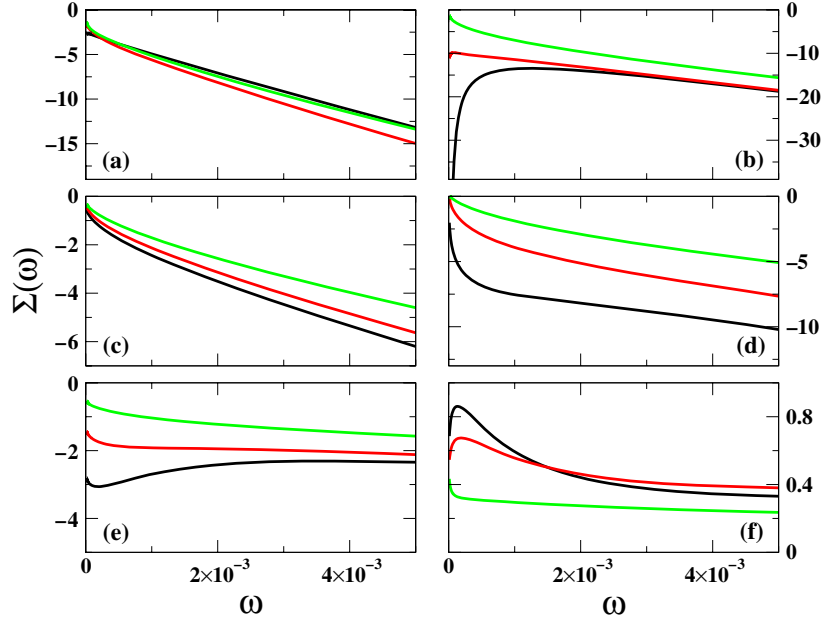


**Figure 12.** Non-vanishing self-energies of the trimer. The three curves correspond to  $\Gamma = 0.5$  (green, lightest line), 0.44 (red, the intermediate dark line) and 0.4 (black, the darkest line). Panels (a)  $\text{Im } \Sigma_{11}(i\omega) = \text{Im } \Sigma_{33}(i\omega)$  and (b)  $\text{Im } \Sigma_{22}(i\omega)$ , for the case of three impurities coupled by the spin exchange  $J$ . Panels (c)  $\text{Im } \Sigma_{11}(i\omega) = \text{Im } \Sigma_{33}(i\omega)$ , (d)  $\text{Im } \Sigma_{22}(i\omega)$ , (e)  $\text{Re } \Sigma_{12}(i\omega) = \text{Re } \Sigma_{32}(i\omega)$  and (f)  $\text{Im } \Sigma_{13}(i\omega)$ , for the case of impurities coupled by a single-particle hopping  $t_{\perp}$ , leading to the same value of  $J$  as before. We used a discretization parameter  $\Lambda = 3.0$ .

very low energy, see panels (c) and (d), although the DOS at site 2 may still display a pseudo-gapped behavior due to the large value of  $\text{Re } \Sigma_{12}(i\omega) = \text{Re } \Sigma_{32}(i\omega)$ .

In conclusion, the dynamical behavior with  $J$  or in the presence of  $t_{\perp}$  is qualitatively similar to the two-impurity cluster.

#### 4. The impurity tetramer

Let us move finally to the last type of cluster investigated, the tetramer drawn in figure 13 with the Hamiltonian

$$\mathcal{H} = \sum_{a=1}^4 \mathcal{H}_a^K + J (\mathbf{S}_1 + \mathbf{S}_3) \cdot (\mathbf{S}_2 + \mathbf{S}_4) + J' (\mathbf{S}_1 \cdot \mathbf{S}_3 + \mathbf{S}_2 \cdot \mathbf{S}_4). \quad (23)$$

This model now describes four spin-1/2 impurities, coupled together by nearest  $J$ , and next nearest neighbor  $J'$ , antiferromagnetic exchanges. In addition, each spin is Kondo coupled to a conduction bath by  $J_K > 0$ . The four baths are once more assumed to be degenerate and particle-hole invariant. As before, the impurities are for convenience only coupled through a spin exchange and not by hopping terms, which we will take into account as perturbations.

##### 4.1. CFT preliminaries for the tetramer

Given our choice of the model (23), the charge degrees of freedom can be still represented by four independent  $SU(2)_1$  CFTs, one for each bath. Concerning the spin degrees of freedom, the

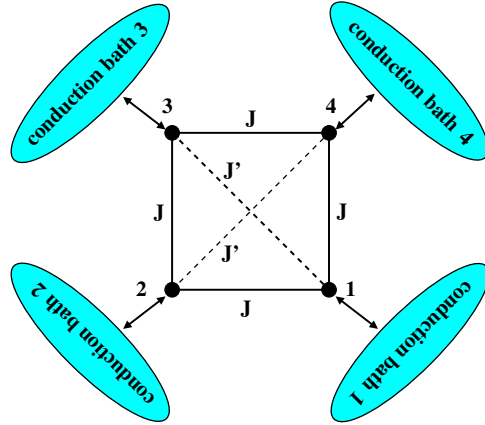


**Figure 13.** The four-impurity cluster.

way in which the impurities are exchange coupled naturally leads to the following conformal embedding scheme

$$\begin{aligned}
 & \left( SU(2)_1^{(1)} \times SU(2)_1^{(3)} \right) \times \left( SU(2)_1^{(2)} \times SU(2)_1^{(4)} \right) \\
 & \rightarrow \left( SU(2)_2^{(1-3)} \times Z_2^{(1)} \right) \times \left( SU(2)_2^{(2-4)} \times Z_2^{(2)} \right) \\
 & \rightarrow SU(2)_4 \times Z_2^{(1)} \times Z_2^{(2)} \times [c = 1 \text{ (CFT)}_{p'=6}]
 \end{aligned} \tag{24}$$

where  $c = 1$  CFT stands for the  $Z_2$  orbifold of a free bosonic CFT (the bosonic field  $\phi$  and  $-\phi$  must be identified) with compactification radius  $R = \sqrt{2p'}$  and  $p' = 6$  [30, 47]. The two step process represented by (24) corresponds to the coupling of the  $SU(2)_1$  spin sectors of the impurities on the diagonals into  $SU(2)_2$ , followed by the coupling of these two new sectors into an  $SU(2)_4$ . The resulting cosets are the two Ising sectors and the  $c = 1$  CFT. The embedding can again be rigorously proven through the character decomposition, but the proof is very technical so we prefer not to give any detail. It is also convenient to represent the two Ising sectors as a single  $c = 1$  free bosonic CFT, now with compactification radius  $R = \sqrt{4}$ , i.e.  $p' = 2$ .

The  $Z_2$  orbifold of a  $c = 1$  CFT with compactification radius  $R = \sqrt{2p'}$  includes, besides the identity, the following primary fields [30, p 785]:

- (i)  $p' - 1$  fields,  $\phi_h$ , with dimensions  $h = \lambda^2/4p'$ , with  $\lambda = 1, \dots, p' - 1$ ;
- (ii) a doubly degenerate field,  $\phi_{p'/4}^{(a)}$ ,  $a = 1, 2$ , with dimension  $p'/4$ ;
- (iii) the twist operators  $\sigma^{(a)}$  and  $\tau^{(a)}$ ,  $a = 1, 2$ , with dimensions  $1/16$  and  $9/16$ , respectively;
- (iv) the dimension-1 operator  $\theta$ .

The fusion rules among the primary fields can be found for instance in [30, p 786].

The embedding

$$SU(2)_2 \times SU(2)_2 \rightarrow SU(2)_4 \times [c = 1 \text{ (CFT)}_{p'=6}], \tag{25}$$

has already been discussed in [48] in the context of the two-impurity two-channel Kondo model. We will see in what follows that some of the anomalies found by those authors do also appear in our model.

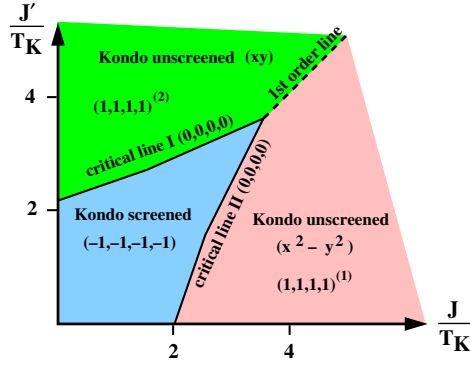


**Figure 14.** Phase diagram of the impurity tetramer described by the Hamiltonian (23). All phases are discussed in the text, and their properties summarized in table 2. Since the calculation is numerically heavy, we had to use a large  $\Lambda = 10$ , which is sufficient to characterize the low energy spectra, hence the various phases, but not adequate to provide accurate estimates of the critical points (for instance, when  $J = 0$ , we find  $(J'/T_K)_* \simeq 0.24$  instead of the two-impurity value  $\simeq 2$  [10]). However, even though the absolute values of the critical  $J/T_K$  and  $J'/T_K$  are underestimated, we still believe that the overall shape of the phase diagram should be representative. For this reason, we have decided to plot the NRG data rescaled in such a way that, when  $J = 0$ , the critical point has the value found in the two-impurity model [10].

**Table 2.** Summary of the main physical properties of the different phases in figure 14.  $\rho(0)$  is the zero-frequency DOS of any of the four impurities,  $\rho_0$  being its non-interacting value. As in table 1, several single-particle operators are considered, specifying whether they are relevant, in which case their dimension is indicated, or not.  $d_i^\dagger d_{i+1}$  and  $d_i^\dagger d_{i+1}^\dagger$  denotes hopping and singlet pairing, respectively, along the sides of the plaquette,  $i-i+1$  meaning 1-2, 2-3, 3-4 or 4-1.  $d_i^\dagger d_{i+2}$  and  $d_i^\dagger d_{i+2}^\dagger$  have the same meaning but along the diagonals, i.e.  $i-i+2$  stands for 1-3 and 2-4.  $x$  is a parameter (not to be confused with the coordinate  $x$  that is used in the first row to identify the different phases, according to figure 14) that changes continuously along the critical lines I and II, reaching at the first-order point along the diagonal  $J = J'$  the value  $x = 1$  for line I and  $x = 2$  for line II.

	$(x^2 - y^2)$	Line II	Screened	Line I	$(xy)$
$\rho(0)/\rho_0$	0	1/2	1	1/2	0
$S_1 - S_2 + S_3 - S_4$	NOT	$1/3 + x^2/6$	NOT	NOT	NOT
$S_1 - S_3$	NOT	NOT	NOT	$1/2 + x^2/2$	NOT
$S_2 - S_4$	NOT	NOT	NOT	$1/2 + x^2/2$	NOT
$d_i^\dagger d_{i+1}$	NOT	$5/8 + (1 - 2x)^2/24$	NOT	NOT	NOT
$d_i^\dagger d_{i+1}^\dagger$	NOT	$5/8 + (1 - 2x)^2/24$	NOT	NOT	NOT
$d_i^\dagger d_{i+2}$	NOT	NOT	NOT	$1/2 + x^2/2$	NOT
$d_i^\dagger d_{i+2}^\dagger$	NOT	NOT	NOT	$1/2 + x^2/2$	NOT

#### 4.2. Fixed points in the tetramer phase diagram

In figure 14, we draw the phase diagram of (23) as obtained by NRG. As before, each fixed point is identified by the  $S$ -matrices  $(S_1, S_2, S_3, S_4)^{(n)}$ , where the superscript  $(n)$  is introduced to distinguish between different fixed points with the same  $S$ -matrices. In table 2 the main physical properties of the different phases are summarized.

4.2.1.  $(S_1, S_2, S_3, S_4) = (-1, -1, -1, -1)$ . This fixed point corresponds to a perfectly Kondo screened phase. It occurs when  $T_K$  is large compared with both  $J$  and  $J'$ . Once again, we will use the Kondo screened  $(-1, -1, -1, -1)$  fixed point as the ancestor BC to generate all the others through fusion.

4.2.2.  $(S_1, S_2, S_3, S_4) = (1, 1, 1, 1)^{(1)}$ . If  $J' = 0$  and  $J \gg T_K$ , the tetramer locks into a non-degenerate singlet state which is obtained by coupling sites 1 and 3 into a triplet, as well as sites 2 and 4, and coupling the two triplets into an overall singlet. This configuration transforms like the function  $x^2 - y^2$  under the  $C_4$  point group of the plaquette, hence the label in figure 14. The singlet decouples from the conduction electrons which do not feel the presence of the impurities anymore, resulting in a phase shift  $\delta = 0$  in every channel. This phase is Fermi liquid-like and remains stable even in the presence of a finite  $J'$ , provided the lowest excitation gap from the ground state of the isolated tetramer is much larger than  $T_K$ . Within CFT, there are several possible fusions which lead the  $(-1, -1, -1, -1)$  fixed point to this new one. One is for instance the fusion with the primary field  $\theta$  of the  $c = 1$  CFT with  $p' = 6$ .

4.2.3.  $(S_1, S_2, S_3, S_4) = (1, 1, 1, 1)^{(2)}$ . If  $J = 0$ , sites 1 and 3 are decoupled from sites 2 and 4, hence the tetramer reduces to two independent Kondo dimers. If  $J' \gg T_K$  each pair of impurities, 1 and 3 or 2 and 4, is strongly bound into a singlet which decouples from the conduction electrons. This impurity configuration transforms like  $xy$  under the  $C_4$  point group, which explains the label in figure 14. This fixed point is obviously stable to a small  $J$  being turned on, hence, in analogy with the dimer, it should be obtainable by the  $(-1, -1, -1, -1)$  fixed point upon fusion with  $\epsilon_1^{(1)} \epsilon_1^{(2)}$ , where  $\epsilon_1^{(a)}$ ,  $a = 1, 2$ , are the energy operator of the two Ising CFTs. This is also the dimension-1 primary field  $\theta$  of the  $c = 1$  CFT with  $p' = 2$ . The NRG spectrum agrees with this prediction not only for small  $J$ , but for the whole region  $J' > J$  with  $J' \gg T_K$ , see figure 14.

4.2.4. *First-order line.* If  $J = J' \gg T_K$ , the tetramer locks into a doubly degenerate spin singlet, the states with symmetry  $x^2 - y^2$  and  $xy$  previously mentioned. The Kondo exchange provides a coupling between these two configurations only at second order, namely via a quartic conduction electron operator, which is therefore irrelevant. Hence the tetramer decouples asymptotically from the conduction baths, and its degeneracy remains untouched. This is confirmed by the NRG calculation, which shows the same Fermi liquid spectrum as in the absence of the impurity cluster apart from each state being doubly degenerate. This phase is the analogous of a first-order line, hence its name in figure 13, with a relevant operator of dimension 0 that describes the splitting of the double degeneracy of the tetramer.

4.2.5.  $(S_1, S_2, S_3, S_4) = (0, 0, 0, 0)^{(1)}$  and  $(0, 0, 0, 0)^{(2)}$ . The Kondo screened phase at small  $J$  and  $J'$  is essentially different from the two unscreened phases at large  $J > J'$  and large  $J' > J$ , respectively. Hence there are two critical lines that start from the  $J' = 0$  axis as well as from the  $J = 0$  one, see figure 14, and finally merge with the first-order line at large  $J = J'$ . This might happen either through a multi-critical point or by a gradual evolution of each line into a first-order critical point. The latter scenario is actually realized, since, unlike in the trimer model, the NRG low energy spectra along both critical lines varies continuously, signaling the existence of marginal perturbations. For the same reason, a precise identification of these critical lines with appropriate boundary CFTs is not a simple task.

Let us start from the simplest case at  $J = 0$ , which corresponds to two independent dimers, sites 1 plus 3 and sites 2 plus 4. The fixed point which separates the Kondo screened phase

from the unscreened one is obviously the superposition of the fixed points of each dimer, discussed previously. It is obtained by the Kondo screened fixed point upon fusion with the product  $\sigma_1^{(1)} \sigma_1^{(2)}$  of the two Ising CFTs [11], and is identified by zero scattering matrices, hence  $(0, 0, 0, 0)^{(2)}$  in figure 14, as well as by a residual  $\ln 2$  entropy. We already showed that the fixed point of a dimer can be destabilized only by the symmetry breaking operators (7)–(9), which are not generated by a small  $J$ . Therefore, a finite  $J \ll J'$  does not spoil the unstable fixed point  $(0, 0, 0, 0)^{(2)}$ , but only moves its position to larger  $J'$ , as it generates a weak ferromagnetic exchange along each dimer. We notice that, upon double fusion,

$$\left(\sigma_1^{(1)} \sigma_1^{(2)}\right) \times \left(\sigma_1^{(1)} \sigma_1^{(2)}\right) = I + \epsilon_1^{(1)} + \epsilon_1^{(2)} + \epsilon_1^{(1)} \epsilon_1^{(2)} \equiv I + \phi_{1/2} + \theta,$$

where the last expression on the right-hand side is written in terms of the corresponding fields of the  $p' = 2, c = 1$  CFT. In agreement with NRG, the operator content includes the marginal operator  $\theta$ , besides the dimension-1/2 relevant operator that moves away from the fixed point. Since for two independent dimers we do know that there is no such marginal operator at the unstable fixed point, we must conclude that  $\theta$  acquires a finite coupling constant only for  $J \neq 0$ . This situation, which is quite exceptional in impurity models, resembles that found in [48] in the two-impurity two-channel Kondo model. An important discovery of [48] was that this marginal operator not only influences the spectrum but also the operator content. Specifically, Georges and Sengupta recognized, by Abelian bosonization of the model, that the fixed point Hamiltonian in the presence of the marginal operator is similar to an x-ray edge problem in bosonization language [49]. Therefore any operator which involves creation or annihilation of the corresponding ‘core–hole’ acquires an additional dimension. It is not difficult to realize that the same happens in our case. Indeed the dimension-1/2 relevant operator can be mapped within bosonization [35] into the operator

$$\epsilon_1^{(1)} + \epsilon_1^{(2)} \rightarrow d^\dagger \Psi(0) + \Psi(0)^\dagger d, \tag{26}$$

which represents the creation (annihilation) of a core–electron,  $d^\dagger(d)$ , and the contemporary annihilation (creation) of a conduction electron at the core–hole site,  $\Psi(0) (\Psi(0)^\dagger)$ . Analogously, the marginal operator transforms like

$$\epsilon_1^{(1)} \epsilon_1^{(2)} \rightarrow (1 - d^\dagger d) \Psi(0)^\dagger \Psi(0),$$

which corresponds to the interaction between the core–hole and the conduction electrons. In the presence of this term, the dimension of the relevant operator (26) changes according to

$$\frac{1}{2} \rightarrow \frac{(2 - 2x)^2}{8},$$

where  $x$  parametrizes the critical line, and is actually related to the phase shift induced by the core–hole in the equivalent x-ray edge problem. Since the end-point at  $J = J'$  is expected to be a first-order one, we conclude that  $x$  moves from 0,  $J = 0$ , to 1,  $J = J'$ , along the critical line. The dimensions of all the other dimension-1/2 symmetry breaking operators changes instead as

$$\frac{1}{2} \rightarrow \frac{1}{2} + \frac{(2x)^2}{8},$$

so that they all become marginal at  $J = J'$ . Notice that, since the twist operators are not affected by the marginal perturbation, the  $S$ -matrices do not change along the line.

Concerning the other critical line,  $(S_1, S_2, S_3, S_4) = (0, 0, 0, 0)^{(1)}$  in figure 14, we find that, when  $J' = 0$ , the NRG spectrum is reproduced with a good approximation by fusing the  $(-1, -1, -1, -1)$  BC with the primary field  $\phi_{1/6}$  of the  $p' = 6, c = 1$  CFT. Once again, since  $\phi_{1/6} \times \phi_{1/6} = I + \theta + \phi_{2/3}$ , the operator content includes, besides the relevant operator

of dimension  $2/3$  that moves away from criticality, the marginal operator  $\theta$  of the  $p' = 6$ ,  $c = 1$  CFT, which explains the continuous evolution of the NRG spectrum from  $J' = 0$  to  $J$ . The role of this marginal operator should be similar to its analogous on the other critical line. Therefore, following the previous analysis and in accordance with [48], we expect the critical line to be parametrized by a ‘phase shift’  $x$  that modifies not only the spectrum but also the operator content. In particular, the dimension of the operator  $\phi_{2/3}$  that moves away from the critical line changes according to

$$\frac{2}{3} \rightarrow \frac{(4 - 2x)^2}{24}.$$

Since this operator eventually acquires vanishing dimension at  $J' \rightarrow J$ , we conclude that  $x \rightarrow 2$  at the end-point. The precise determination of  $x$  along the line is however difficult to extract from our NRG spectra.

At  $x = 0$ , the most relevant symmetry breaking operator would correspond to the staggered magnetization

$$\mathbf{J}_1 - \mathbf{J}_2 + \mathbf{J}_3 - \mathbf{J}_4, \quad (27)$$

with dimension  $1/3$ , which, at finite  $x$ , changes into

$$\frac{1}{3} + \frac{(2x)^2}{24},$$

hence becomes marginal at  $J = J'$ . This is physically sound, since at  $J = J'$  there is maximum spin frustration. Besides the staggered magnetization, there are other less relevant symmetry breaking operators of dimension  $2/3$  at  $x = 0$ . One of them is the singlet four-fermion operator

$$(\mathbf{J}_1 - \mathbf{J}_3) \cdot (\mathbf{J}_1 - \mathbf{J}_2 + \mathbf{J}_3 - \mathbf{J}_4) + (1, 3) \leftrightarrow (2, 4),$$

whose dimension at  $x \neq 0$  is  $1/2 + (2 + 2x)^2/24$ , thus becoming soon irrelevant.

The other symmetry breaking operators of dimension  $2/3$  correspond actually to all possible mean field decoupling schemes of the exchange term

$$(\mathbf{J}_1 + \mathbf{J}_3) \cdot (\mathbf{J}_2 + \mathbf{J}_4),$$

into inter-bath single-particle operators. Among them, we just mention the inter-bath hopping,

$$\sum_{\sigma} (c_{1\sigma}^{\dagger} + c_{3\sigma}^{\dagger})(c_{2\sigma} + c_{4\sigma}) + \text{H.c.},$$

as well as the d wave Cooper pairing,

$$(c_{1\uparrow}^{\dagger} - c_{3\uparrow}^{\dagger})(c_{2\downarrow} - c_{4\downarrow}) - (\uparrow \leftrightarrow \downarrow).$$

They are all degenerate and, at  $x \neq 0$ , have dimension

$$\frac{5}{8} + \frac{(1 - 2x)^2}{24}.$$

At  $x = 2$  they become marginal, but, interestingly enough, their dimension is non-monotonic in  $x$ , although always greater than the staggered magnetization (27). Along this line, too, the  $S$ -matrices and the residual entropy remain constant and equal to  $(S_1, S_2, S_3, S_4) = (0, 0, 0, 0)$  and  $\ln 2$ , respectively.

Like in the dimer and trimer examples, the relevance of the inter-bath hopping implies that both critical lines are no more accessible if, instead of four impurities coupled by a spin exchange, one considers four impurities coupled by a single-particle hopping, which is the actual situation within cluster DMFT. Unfortunately, in this case we cannot obtain reliable spectral functions by NRG because of numerical limitations. Therefore, we cannot verify whether, in spite of the fact that the critical point is washed out, a sizable critical region still

survives. However we tend to believe that it is the case, just like in the previous examples. Finally, since both critical lines are stable towards the conventional particle–hole symmetry breaking, the phase diagram for  $J \neq J'$ , as function of  $U/\Gamma$  and of the average impurity occupancy, still looks like the dimer one, see figure 5.

## 5. Discussion and conclusions

In this review, we attempted to uncover the key features that distinguish Anderson impurity clusters from single-impurity models and that could play an important role within cluster dynamical mean field theory as opposed to its original single-site formulation. All the examples that we have studied, namely two-, three- and four-impurity clusters, share very similar properties.

In particular, if the impurities within the cluster are coupled to one another by a two-body spin exchange while each of them is hybridized with its own separate conduction bath, the phase diagrams as function of the average impurity occupancy and of the Hubbard  $U$  are practically the same, see figure 5. For  $U/\Gamma$  less than a critical value, perfect Kondo screening occurs and the impurity cluster spectral functions show the conventional Kondo resonance. Above that critical value, the inter-impurity exchange prevails instead and takes care of freezing out the impurity degrees of freedom. Here, the impurity spectral functions develop a pseudo-gap at the chemical potential, which is gradually filled in by ‘doping’, i.e., by moving the average impurity occupancy away from half-filling. These two regimes are separated by a critical line that is identified by several instability channels. In all cases, the instability channels correspond to all possible mean field decoupling schemes of the spin exchange into bilinear operators. They include the intra-bath magnetization, staggered according to the signs and relative strengths of the spin exchange constants, and all singlet inter-bath bilinear operators, like the inter-bath hoppings or singlet Cooper pairs. The trend from the dimer towards the tetramer is towards a prevailing instability in the staggered magnetization channel. The dynamics across the critical point are basically controlled by two separate energy scales. One of them, which we denoted as  $T_+$ , is finite across the transition and roughly of the order of the spin exchange. The other,  $T_-$ , is the scale generated by the deviation  $X$  from the critical line. It vanishes as  $T_- \sim |X|^\alpha$ , where, in the most interesting case of the tetramer, the exponent  $1 \leq \alpha \leq 3$ , is non-universal and depends on the frustration. From the point of view of the impurity spectral functions, see e.g. figure 6,  $T_+$  is the width of a broad incoherent peak within the Hubbard side-bands, smooth across the critical point. On the contrary,  $T_-$  is the width of the Kondo-like resonance that develops on top of the broader one, in the Kondo screened phase. As the critical point is approached, the Kondo resonance becomes narrower, and eventually disappears right at the critical point, leaving behind only the incoherent peak. In the unscreened phase,  $T_-$  controls the width of the pseudo-gap that opens inside the incoherent part.

If the impurities inside a cluster are coupled one another by a single-particle hopping,  $t_\perp$ , instead of a spin exchange, the transition turns into a crossover from the Kondo resonance behavior to the pseudo-gapped one. Indeed, the inter-impurity hopping plays a double role. On the one hand it generates, for large  $U$ , a spin exchange,  $J = 4t_\perp^2/U$ , that might drive the model across the critical point. On the other hand, it also induces a small inter-bath hybridization,  $V \sim J_K t_\perp/U$ , that is a relevant perturbation and destabilizes the critical point. Specifically,  $V$  cuts off all critical point singularities below an energy scale  $E_{\text{cut-off}} \sim V^\beta$ , where  $\beta \geq 3$  in the tetramer and  $\beta = 2$  in the dimer. Since  $V$  is small and  $\beta$  large, we expect that, in spite of the critical point being no longer accessible, a ‘critical region’ should still survive if  $E_{\text{cut-off}} \ll T_+ \sim J$ . We indeed found evidences in favor of this scenario both in the dimer as well as in the trimer, where the impurity spectral functions are numerically accessible.

Coming back to our original scope, let us imagine that we implement a cluster DMFT simulation of a Hubbard model using a dimer, a trimer or a tetramer as representative clusters. As  $U$  increases driving the model towards the Mott transition, the effective impurity cluster must necessarily go through the above mentioned critical region (even if a true criticality is, rigorously speaking, not accessible since the impurities as well as the baths are coupled by a single-particle hopping). In this region, the instability channels of the avoided critical point will be amplified and, after the DMFT self-consistency, can induce a true bulk instability in the lattice model. At half-filling, our results on the impurity clusters suggest that most likely magnetism appears, even in the presence of frustration. However, since instabilities in particle-hole channels are weakened or removed by doping away from commensurate fillings, while that weakening does not happen in particle-particle channels, a superconducting dome may emerge near half-filling. Indeed, recent cluster DMFT simulations of the Hubbard model on a square lattice [50, 51] found evidence of a d wave superconducting phase away from half-filling, in close analogy with the phase diagram of high  $T_c$  superconductors.

Nevertheless, irrespectively of which symmetry broken phase actually occurs at low temperatures, the physics of impurity clusters suggests that, in the normal phase above a critical temperature, the transition to the Mott insulator is accompanied by the gradual opening of a pseudo-gap in the single-particle spectral function. In this pseudo-gapped region, Fermi liquid behavior, i.e.  $\Sigma(i\omega) \sim i\omega$ , is recovered only at extremely low energies, suggesting the existence of a finite temperature non-Fermi liquid behavior. Evidence in favor of this scenario has been found in a recent cluster DMFT simulation of a paramagnetic two-dimensional Hubbard model [52].

Another aspect worth emphasizing concerns the behavior of the Drude weight in the metal away from half-filling across the symmetry breaking phase transition. From the point of view of the effective impurity model, a symmetry breaking in the conduction baths opens up new screening channels that can rid the impurity of its residual entropy at the critical point. This in turns leads to an increase in screening energy gain that, translated back into the lattice model, implies an increase in band energy gain, i.e. of the Drude weight. This behavior is actually the fingerprint of this kind of instability that reflects the underlying impurity critical point, as opposed to the conventional Stoner or BCS instability that are accompanied by a decrease of Drude weight. The increase of Drude weight has been indeed observed in DMFT simulations of the two-dimensional Hubbard model [50] as well as of a two-band Hubbard model [32] that maps, within DMFT, onto the impurity dimer.

## Acknowledgments

We acknowledge helpful discussions with E Tosatti. We are very grateful to A Georges, who brought to our attention [48] which has been enlightening for our study.

## Appendix. CFT at work

In this appendix, we show how *conformal embedding* works in a few simple examples. We do it through the identification of the partition function, the so-called *character decomposition*.

The first step of bosonization in one dimension is the linearization of the free electron spectrum around the Fermi momentum [35]. This linearization is not expected to affect the low energy behavior provided the perturbations are weak compared to the bandwidth. Therefore let us consider, instead of a tight binding model, free spinless Dirac fermions, which have indeed a linear spectrum, on a chain of length  $L$  with anti-periodic boundary conditions. We are going to

consider Dirac fermions moving only in one direction, namely with a single chirality, because this is the case relevant to a semi-infinite chain where the single-particle wavefunctions with negative momenta are not independent from those with positive ones.

The single-particle wavefunctions for a chiral Dirac fermion are plane waves with momentum

$$k = \frac{\pi}{L} (2n - 1),$$

$n$  being integer. The Hamiltonian in momentum space reads

$$\mathcal{H} = v_F \sum_k k c_k^\dagger c_k, \quad (\text{A.1})$$

where  $v_F$  has to be identified with the Fermi velocity of the original tight binding model. Let us define, for positive  $k$ ,

$$\begin{aligned} \alpha_k &= c_k, \\ \beta_k &= c_{-k}^\dagger, \end{aligned}$$

so that, apart from an (actually infinite) constant, the Hamiltonian becomes

$$\mathcal{H} = v_F \sum_{k>0} k \left( \alpha_k^\dagger \alpha_k + \beta_k^\dagger \beta_k \right). \quad (\text{A.2})$$

The partition function at temperature  $T$  is simply

$$Z_{\text{Dirac}} = \prod_{k>0} [1 + \exp(-\beta v_F k)]^2 = \prod_{n \geq 1} (1 + q^{n-1/2})^2, \quad (\text{A.3})$$

where conventionally [30]  $q$  is defined as

$$q = \exp\left(-\beta \frac{2\pi v_F}{L}\right) \equiv e^{2\pi i \tau}.$$

One can show that

$$Z_{\text{Dirac}}(q) = \frac{\theta_3(q)}{\varphi(q)}, \quad (\text{A.4})$$

where  $\theta_3$  is the third Jacobi theta function

$$\theta_3(q) = \sum_{n=-\infty}^{\infty} q^{n^2/2},$$

and  $\varphi$  the Euler function

$$\varphi(q) = \prod_{n \geq 1} (1 - q^n).$$

On the other hand, it is known by bosonization [35] that, for positive  $p = 2\pi n/L > 0$ , the operators

$$b_p = -i \sqrt{\frac{2\pi}{pL}} \rho(p) = -i \sqrt{\frac{2\pi}{pL}} \sum_k c_k^\dagger c_{k+p}, \quad b_p^\dagger = i \sqrt{\frac{2\pi}{pL}} \rho(-p),$$

satisfy bosonic commutation relations. In addition their equation of motion can be reproduced by the Hamiltonian

$$\mathcal{H} = \frac{\pi v_F}{L} \sum_p \rho(p) \rho(-p) = v_F \sum_{p>0} p b_p^\dagger b_p + \frac{\pi v_F}{L} \Delta N^2, \quad (\text{A.5})$$

where it is assumed that  $\rho(p = 0)$  is the variation  $\Delta N$  of the electron number with respect to a reference value. The partition function of this bosonic model is the product of the free boson term

$$\prod_{p>0} [1 - \exp(-\beta v_F p)]^{-1} = \prod_{n>0} (1 - q^n)^{-1} = \varphi(q)^{-1}$$

plus the contribution of  $\Delta N$  which is, assuming an infinite reference number,

$$\sum_{n=-\infty}^{\infty} \exp\left(-\beta \frac{v_F \pi}{L} n^2\right) = \sum_{n=-\infty}^{\infty} q^{n^2/2} = \theta_3(q).$$

One immediately recognizes that the bosonic partition function coincides with the fermionic one.

We can proceed further on, and consider spinful Dirac fermions. Obviously, the partition function is the square of  $Z_{\text{Dirac}}$  in equation (A.4). As the simplest example of *conformal embedding* and *character decomposition*, we consider a perturbation that only preserves independently the spin  $SU(2)$  symmetry and the charge isospin  $SU(2)$ , defined through the generators  $\mathbf{I}$ , which are the  $q = 0$  components of the so-called isospin current operators

$$\begin{aligned} I_z(q) &= \frac{1}{2} \sum_{k\sigma} \left( c_{k\sigma}^\dagger c_{k+q\sigma} - \delta_{q0} \right), \\ I^+(q) &= \sum_k c_{k\uparrow}^\dagger c_{-k-q\downarrow}^\dagger, \\ I^-(q) &= (I^+)^\dagger. \end{aligned}$$

The spin  $SU(2)$  current operators are instead

$$\mathbf{S}(q) = \frac{1}{2} \sum_{k\alpha\beta} c_{k\alpha}^\dagger \boldsymbol{\sigma}_{\alpha\beta} c_{k+q\beta}, \tag{A.6}$$

where  $\boldsymbol{\sigma}$  are the Pauli matrices. In real space these current operators,  $J_a = I_a, S_a$ , satisfy the commutation relations

$$[J_a(x), J_b(y)] = i\epsilon_{abc} \delta(x - y) J_c(x) - ik \frac{1}{4\pi} \delta_{ab} \frac{\partial \delta(x - y)}{\partial x},$$

with  $k = 1$ . For generic  $k \geq 1$ , the above commutation relations identify an  $SU(2)_k$  CFT [30], where the label  $k$  may be regarded as the number of channels which are used to build up the generators. An  $SU(2)_k$  CFT has primary fields  $\phi_{2j}^{(k)}$  with spin quantum numbers  $j$ , such that  $2j = 0, 1, \dots, k$ . Their dimensions are  $x_j = j(j + 1)/(k + 2)$ . The product of two primary fields with spin  $j$  and  $j'$  yields all primary fields with spin between  $|j - j'|$  and  $\min(k - j - j', j + j')$ . The Hilbert space of the theory is obtained by applying the primary fields on the reference vacuum state and, from this ancestor state, by generating all descendant states applying the current operators with  $q < 0$ . This is what is called a *conformal tower* [30]. The energy difference between the descendant states and their ancestor is an integer multiple of the fundamental level spacing  $\Delta = 2\pi v_F/L$ . The character  $\chi_{2j}^{(k)}$  represents the contribution to the partition function of the conformal tower generated by the primary field  $\phi_{2j}^{(k)}$  [30].

This construction may look abstruse but actually has a simple physical interpretation. Let us consider again a single spinful fermion,  $k = 1$ . Let us further assume that on average the number of electrons is equal to the number of sites, and the latter is even. In this case the ground state is obtained by filling with two electrons of opposite spin all single-particle levels below the chemical potential, which lies in the middle of two consecutive single-particle levels separated by the fundamental spacing  $\Delta$ , from now on our energy unit. With this definition, the Hilbert space can be constructed as follows. One can start from the vacuum and act on it

**Table A.1.** The spectrum of spinful electrons when the ground state contains an even number of particles.

$I$	$S$	$x$
0	0	0
1/2	1/2	1/2

with particle–hole excitations, namely with  $I_z(q)$  or  $S(q)$  with  $q < 0$ . In addition, one can apply the operators  $I^+(q)$  or  $I^-(q)$ , again with  $q < 0$ , to change by an even multiple the number of electrons, and then consider all particle–hole excitations on top of these states. In this way, one obtains all states which have even number of electrons, like the vacuum state. This is nothing but the conformal towers obtained by the ancestor fields  $\phi_0^{(1)}$  in both the charge and spin  $SU(2)_1$  sectors, which should therefore contribute to the partition function with the product of characters  $(\chi_0^{(1)})_{\text{charge}}(\chi_0^{(1)})_{\text{spin}}$ .

The rest of the Hilbert space includes all states with odd number of electrons. Since a single electron carries isospin and spin 1/2, all these states have half-odd integer values of  $I_z$  and  $S_z$ . One realizes that they can all be obtained by applying the product of the isospin and spin primary fields  $\phi_1^{(1)}_{\text{charge}} \times \phi_1^{(1)}_{\text{spin}}$ , which is nothing but the single-electron operator, and construct out of it all descendant states. Their contribution to the partition function should then be  $(\chi_1^{(1)})_{\text{charge}}(\chi_1^{(1)})_{\text{spin}}$ . The expression of the  $SU(2)_k$  characters [30, p 586] is

$$\chi_l^{(k)}(q) = \frac{1}{\eta(q)^3} \sum_{n=-\infty}^{\infty} [2n(k+2) + l + 1] q^{(2n(k+2)+l+1)^2/4(k+2)},$$

where

$$\eta(q) = q^{1/24} \varphi(q),$$

is the Dedekind function. In the specific case of  $k = 1$ ,

$$\chi_0^{(1)}(q) = \sqrt{\frac{\theta_3(q)^2 + \theta_4(q)^2}{2\eta(q)^2}},$$

$$\chi_1^{(1)}(q) = \sqrt{\frac{\theta_3(q)^2 - \theta_4(q)^2}{2\eta(q)^2}},$$

where

$$\theta_4(q) = \sum_{n=-\infty}^{\infty} (-1)^n q^{n^2/2},$$

is the fourth Jacobi theta function. Hence we find that

$$\left(\chi_0^{(1)}\right)_{\text{charge}} \left(\chi_0^{(1)}\right)_{\text{spin}} + \left(\chi_1^{(1)}\right)_{\text{charge}} \left(\chi_1^{(1)}\right)_{\text{spin}} = \frac{\theta_3(q)^2}{\eta(q)^2} = q^{-1/12} Z_{\text{Dirac}}(q)^2, \tag{A.7}$$

which, apart from the vacuum polarization contribution  $q^{-1/12}$ , is exactly the partition function of two species of Dirac fermions. The spectrum, and correspondingly the partition function, can be represented as in table A.1. In that and all forthcoming tables, we identify each conformal tower by the quantum numbers of the primary fields which generate the ancestor states.  $x$  is the energy in units of  $\Delta$  of the ancestor state with respect to the chemical potential. The descendant levels of an ancestor have energies  $x + n$ , with  $n$  a positive integer. Notice that an important consequence of conformal invariance is that the energy of each state in units of  $\Delta$  coincide with the dimension of the operator which, applied to the vacuum, yields that state.

**Table A.2.** The spectrum of spinful electrons when the ground state contains an odd number of particles.

$I$	$S$	$x - 1/4$
1/2	0	0
0	1/2	0

Following the same reasoning, one can easily show that the table of the energy spectrum in the case of odd chains at half-filling (i.e. odd average number of electrons) is the one of table A.2. The ground state is fourfold degenerate, the chemical potential coinciding with a single-particle level. One can readily realize that the even and odd chain spectra can be turned one into the other by *fusion* with a charge or a spin primary field  $\phi_1^{(1)}$ . This is the physics of the single-channel spin-1/2 Kondo impurity model. Indeed, when Kondo effect is established, the impurity site becomes effectively a new site of the chain, thus changing the parity of the number of sites, i.e. the boundary conditions.

*The two-channel model.* Let us consider a more involved *conformal embedding* in the case of two channels of spinful fermions. The partition function is the square of the partition function (A.7) of a single channel, and can be written for even chains as

$$Z = \sum_{n_1, n_2=0,1} (\chi_{n_1}^{(1)} \chi_{n_2}^{(1)})_{\text{charge}} (\chi_{n_1}^{(1)} \chi_{n_2}^{(1)})_{\text{spin}}, \tag{A.8}$$

where  $n_1$  refers to channel 1 and  $n_2$  to channel 2. For odd chains, one readily finds that

$$Z = \sum_{n_1, n_2=0,1} (\chi_{n_1}^{(1)} \chi_{n_2}^{(1)})_{\text{charge}} (\chi_{1-n_1}^{(1)} \chi_{1-n_2}^{(1)})_{\text{spin}}. \tag{A.9}$$

These expressions manifestly show that the two-channel free conduction electrons are invariant under independent spin or isospin  $SU(2)$  transformations within each channel, namely under a large symmetry  $SU(2) \times SU(2) \times SU(2) \times SU(2)$ .

Let us suppose that the impurity couples only to the spin current operators in such a way that only the overall  $SU(2)$  spin symmetry is preserved. Therefore, while the charge degrees of freedom can still be represented by two  $SU(2)_1$  CFT's, the appropriate conformal embedding for the spin sectors should involve an  $SU(2)_2$  CFT, since the total spin current is made up of two channels, times the coset CFT, namely

$$SU(2)_1 \times SU(2)_1 \rightarrow SU(2)_2 \times \frac{SU(2)_1 \times SU(2)_1}{SU(2)_2}.$$

Since the central charge is conserved and each  $SU(2)_k$  has a central charge  $3k/(k + 2)$ , the coset theory should have  $c = 1/2$ , which corresponds to the central charge of an Ising CFT. This can be proved rigorously by the *character decomposition*.

The Ising CFT has three primary fields, the identity  $I$ , with dimension 0, the energy field  $\epsilon$ , with dimension 1/2, and the spin field  $\sigma$  with dimension 1/16. The fusion rules are [30]

$$\begin{aligned} I \times I &= I, & \epsilon \times \epsilon &= I, & \sigma \times \sigma &= I + \epsilon, & I \times \epsilon &= \epsilon, \\ I \times \sigma &= \sigma, & \epsilon \times \sigma &= \sigma. \end{aligned} \tag{A.10}$$

The characters  $\chi_x^I$ , where  $x$  is the dimension of the primary field, are given by (all functions are assumed to depend on the variable  $q$ , even when not indicated)

$$\chi_0^I = \frac{1}{2} \left[ \sqrt{\frac{\theta_3}{\eta}} + \sqrt{\frac{\theta_4}{\eta}} \right],$$

**Table A.3.** The spectra of two channels on even chains, left table, and odd chains, right table.  $I_1$  and  $I_2$  are the isospin value of each channel,  $S$  the value of the total spin and Ising refers to the Ising primary fields.

$I_1$	$I_2$	$S$	Ising	$x$	$I_1$	$I_2$	$S$	Ising	$x - 1/2$
0	0	0	0	0	0	0	0	1/2	0
0	0	1	1/2	1	0	0	1	0	0
1/2	0	1/2	1/16	1/2	1/2	0	1/2	1/16	0
0	1/2	1/2	1/16	1/2	0	1/2	1/2	1/16	0
1/2	1/2	0	1/2	1	1/2	1/2	0	0	0
1/2	1/2	1	0	1	1/2	1/2	1	1/2	1

**Table A.4.** Left table: the spectrum of the unstable fixed point of the two spin-1/2 Kondo impurity model. Right table: the boundary operator dimensions at the unstable fixed point. The single and double asterisks identify, respectively, the symmetry invariant and symmetry breaking relevant physical operators.

$I_1$	$I_2$	$S$	Ising	$x - 1/16$	$I_1$	$I_2$	$S$	Ising	$x$
0	0	0	1/16	0	0	0	0	0	0
1/2	0	1/2	0	3/8	0	0	0	1/2	1/2 <sup>(*)</sup>
0	1/2	1/2	0	3/8	1/2	0	1/2	1/16	1/2
0	0	1	1/16	1/2	0	1/2	1/2	1/16	1/2
1/2	1/2	0	1/16	1/2	0	0	1	0	1/2 <sup>(**)</sup>
1/2	0	1/2	1/2	7/8	1/2	1/2	0	0	1/2 <sup>(**)</sup>
0	1/2	1/2	1/2	7/8	0	0	1	1/2	1
1/2	1/2	1	1/16	1	1/2	1/2	0	1/2	1
					1/2	1/2	1	0	1
					1/2	1/2	1	1/2	3/2

$$\chi_{1/2}^I = \frac{1}{2} \left[ \sqrt{\frac{\theta_3}{\eta}} - \sqrt{\frac{\theta_4}{\eta}} \right],$$

$$\chi_{1/16}^I = \sqrt{\frac{1}{2}} \sqrt{\frac{\theta_2}{\eta}},$$

where the second Jacobi function is defined by

$$\theta_2 = \sum_{n=-\infty}^{\infty} q^{(n-1/2)^2/2}.$$

One can show that the product of characters of two  $SU(2)_1$  CFTs,  $\chi_{2j}^{(1)} \chi_{2j'}^{(1)}$ , can be related to the product of characters of an  $SU(2)_2$  and an Ising CFTs,  $\chi_{2l}^{(2)} \chi_x^I$ , by

$$\chi_0^{(1)} \chi_0^{(1)} = \chi_0^{(2)} \chi_0^I + \chi_2^{(2)} \chi_{1/2}^I,$$

$$\chi_0^{(1)} \chi_1^{(1)} = \chi_1^{(1)} \chi_0^{(1)} = \chi_1^{(2)} \chi_{1/16}^I,$$

$$\chi_1^{(1)} \chi_1^{(1)} = \chi_0^{(2)} \chi_{1/2}^I + \chi_2^{(2)} \chi_0^I.$$

By means of the above decomposition one can write the tables of the spectra for even and odd chains, as given in table A.3. By these tables one easily realizes that the spectrum of even chains can be turned into that of odd chains, and vice versa, either by fusion with the  $SU(2)_2$  primary field of spin 1, or by fusion with the Ising field  $\epsilon$ . As we mention in section 2, the unstable fixed point of the two spin-1/2 Kondo impurity model was found by Affleck and Ludwig [11, 12] to correspond to fusion with the Ising field  $\sigma$ . If one performs such a fusion in

the spectra of table A.3, one obtains, by means of the fusion rules (A.10), a new spectrum that was shown to reproduce the NRG spectrum obtained by Jones and Varma [10]. By performing a further fusion (so-called *double fusion* [39, 40]) with  $\sigma$ , one determines the dimensions of the boundary operators at the unstable fixed point, shown in the same table A.4. Their physical meaning is discussed in section 2.

## References

- [1] Mott N F 1949 The basis of the electron theory of metals, with special reference to the transition metals *Proc. Phys. Soc. (London)* **62** 416
- [2] Mott N F 1990 *Metal Insulator Transition* (London: Taylor and Francis)
- [3] Misguich G and Lhuillier C 2005 Two-dimensional quantum antiferromagnets *Frustrated Spin Systems* ed H T Diep (Singapore: World-Scientific) p 981 and references therein
- [4] Hewson A C 1997 *The Kondo Problem to Heavy Fermions* (Cambridge: Cambridge University Press)
- [5] Millis A J 1993 Effect of a nonzero temperature on quantum critical points in itinerant fermion systems *Phys. Rev. B* **48** 7183
- [6] Coleman P, Pepin C, Si Q and Ramazashvili R 2001 How do Fermi liquids get heavy and die? *J. Phys.: Condens. Matter* **13** 723
- [7] Si Q 2004 Quantum critical metals: beyond the order parameter fluctuations *Adv. Solid State Phys.* **44** 253
- [8] Jones B A and Varma C M 1987 Study of two magnetic impurities in a Fermi gas *Phys. Rev. Lett.* **58** 843
- [9] Jones B A, Varma C M and Wilkins J W 1988 Low-temperature properties of the two-impurity Kondo Hamiltonian *Phys. Rev. Lett.* **61** 125
- [10] Jones B A and Varma C M 1989 Critical point in the solution of the two magnetic impurity problem *Phys. Rev. B* **40** 324
- [11] Affleck I and Ludwig A W W 1992 Exact critical theory of the two-impurity Kondo model *Phys. Rev. Lett.* **68** 1046
- [12] Affleck I, Ludwig A W W and Jones B A 1995 Conformal-field-theory approach to the two-impurity Kondo problem: comparison with numerical renormalization-group results *Phys. Rev. B* **52** 9528
- [13] Paul B C and Ingersent K 1996 Frustration-induced non-Fermi-liquid behavior in a three-impurity Kondo Model arXiv: [cond-mat/9607190v1](https://arxiv.org/abs/cond-mat/9607190v1)
- [14] Ingersent K, Ludwig A W W and Affleck I 2005 Kondo screening in a magnetically frustrated nanostructure: exact results on a stable, non-Fermi-liquid phase *Phys. Rev. Lett.* **95** 257204
- [15] Affleck I and Ludwig A W W 1991 The Kondo effect, conformal field theory and fusion rules *Nucl. Phys. B* **352** 849–62
- [16] Affleck I and Ludwig A W W 1991 Critical theory of overscreened Kondo fixed points *Nucl. Phys. B* **360** 641–96
- [17] Jamneala T, Madhavan V and Crommie M F 2001 Kondo response of a single antiferromagnetic chromium trimer *Phys. Rev. Lett.* **87** 256804
- [18] Kudasov Yu B and Uzdin V M 2002 Kondo state for a compact Cr trimer on a metallic surface *Phys. Rev. Lett.* **89** 276802
- [19] Savkin V V, Rubtsov A N, Katsnelson M I and Lichtenstein A I 2005 Correlated adatom trimer on metal surface: a continuous time quantum Monte Carlo study *Phys. Rev. Lett.* **94** 026402
- [20] Lazarovits B, Simon P, Zarand G and Szunyogh L 2005 Exotic Kondo effect from magnetic trimers *Phys. Rev. Lett.* **95** 077202
- [21] Georges A, Kotliar G, Krauth W and Rozenberg M J 1996 Dynamical mean-field theory of strongly correlated fermion systems and the limit of infinite dimensions *Rev. Mod. Phys.* **68** 13
- [22] Kotliar G, Savrasov S Y, Pálsson G and Biroli G 2001 Cellular dynamical mean field approach to strongly correlated systems *Phys. Rev. Lett.* **87** 186401
- [23] Maier T, Jarrell M, Pruschke T and Hettler M H 2005 Quantum cluster theories *Rev. Mod. Phys.* **77** 1027
- [24] Senechal D, Perez D and Pioro-Ladriere M 2000 The spectral weight of the Hubbard model through cluster perturbation theory *Phys. Rev. Lett.* **84** 522
- [25] Potthoff M, Aichhorn M and Dahnken C 2003 Variational cluster approach to correlated electron systems in low dimensions *Phys. Rev. Lett.* **91** 206402
- [26] Lichtenstein A I and Katsnelson M I 2000 Antiferromagnetism and d-wave superconductivity in cuprates: a cluster dynamical mean-field theory *Phys. Rev. B* **62** R9283–6
- [27] Wilson K G 1975 The renormalization group: critical phenomena and the Kondo problem *Rev. Mod. Phys.* **47** 773

- [28] Krishnamurthy H R, Wilkins J W and Wilson K G 1980 Renormalization-group approach to the Anderson model of dilute magnetic alloys. I. Static properties for the symmetric case *Phys. Rev. B* **21** 1003
- [29] Krishnamurthy H R, Wilkins J W and Wilson K G 1980 Renormalization-group approach to the Anderson model of dilute magnetic alloys. II. Static properties for the asymmetric case *Phys. Rev. B* **21** 1044
- [30] Di Francesco P, Mathieu P and Sénéchal D 1996 *Conformal Field Theory* (Berlin: Springer)
- [31] Capone M, Fabrizio M, Castellani C and Tosatti E 2002 Strongly correlated superconductivity *Science* **296** 2364
- [32] Capone M, Fabrizio M, Castellani C and Tosatti E 2004 Strongly correlated superconductivity and pseudogap phase near a multiband Mott insulator *Phys. Rev. Lett.* **93** 047001
- [33] Fabrizio M, Ho A F, De Leo L and Santoro G E 2003 Nontrivial fixed point in a twofold orbitally degenerate Anderson impurity model *Phys. Rev. Lett.* **91** 246402
- [34] De Leo L and Fabrizio M 2004 Spectral properties of a two-orbital Anderson impurity model across a non-Fermi-liquid fixed point *Phys. Rev. B* **69** 245114
- [35] Gogolin A O, Nersisyan A A and Tsvetlik A M 1998 *Bosonization and Strongly Correlated Systems* (Cambridge: Cambridge University Press)
- [36] Belavin A A, Polyakov A M and Zamolodchikov A B 1984 Infinite conformal symmetry in two-dimensional quantum field theory *Nucl. Phys. B* **241** 333–80
- [37] Knizhnik V G and Zamolodchikov A B 1984 Current algebra and Wess–Zumino model in two dimensions *Nucl. Phys. B* **247** 83–103
- [38] Cardy J L 1986 Operator content of two-dimensional conformally invariant theories *Nucl. Phys. B* **270** 186–204
- [39] Cardy J L 1989 Boundary conditions, fusion rules and the Verlinde formula *Nucl. Phys. B* **324** 581
- [40] Affleck I 1995 Conformal field theory approach to the Kondo effect *Acta Phys. Polon. B* **26** 1869
- [41] Nozières P 1974 A Fermi liquid description of Kondo effect at low temperatures *J. Low Temp. Phys.* **17** 31
- [42] Blume M 1966 Theory of the first-order magnetic phase change in  $\text{UO}_2$  *Phys. Rev.* **141** 517
- [43] Capel H W 1966 On possibility of first-order phase transitions in Ising systems of triplet ions with zero-field splitting *Physica* **32** 866
- [44] Affleck I and Ludwig A W W 1991 Universal noninteger ‘ground state degeneracy’ in critical quantum systems *Phys. Rev. Lett.* **67** 161–4
- [45] Affleck I and Ludwig A W W 1993 Exact conformal-field-theory results on the multichannel Kondo effect: single-fermion Green’s function, self-energy, and resistivity *Phys. Rev. B* **48** 7297
- [46] Affleck I, Ludwig A W W, Pang H-B and Cox D L 1992 Relevance of anisotropy in the multichannel Kondo effect: comparison of conformal field theory and numerical renormalization-group results *Phys. Rev. B* **45** 7918
- [47] Affleck I, Oshikawa M and Saleur H 2001 Quantum brownian motion on a triangular lattice and  $c = 2$  boundary conformal field theory *Nucl. Phys. B* **594** 535
- [48] Georges A and Sengupta A 1995 Solution of the 2-impurity 2-channel Kondo model *Phys. Rev. Lett.* **74** 2808
- [49] Schotte K and Schotte U 1969 Tomonaga’s model and the threshold singularity of x-ray spectra of metals *Phys. Rev.* **182** 479
- [50] Maier T A, Jarrell M, Schulthess T C, Kent P R C and White J B 2005 Systematic study of d-wave superconductivity in the 2d repulsive Hubbard model *Phys. Rev. Lett.* **95** 237001
- [51] Capone M and Kotliar G 2006 Competition between d-wave superconductivity and antiferromagnetism in the 2d Hubbard model arXiv: [cond-mat/0603227v1](https://arxiv.org/abs/cond-mat/0603227v1)
- [52] Zhang Y Z and Imada M 2007 Pseudogap and Mott transition studied by cellular dynamical mean field theory arXiv: [0706.0444v1](https://arxiv.org/abs/0706.0444v1)